UNIVERSITE DE NANTES
POLYTECH NANTES

Aalto University
School of Electrical
Engineering

Internship 4A

Control grid following, grid forming and fault testing of Wind Farm Equipped with Type IV Generator

Student:
Pierre Troussard

Internship supervisor:
Anouar Belahcen

Internship advisor:
Martin Floran

University's Coordinator:
Yasser Diab

date: May 20 to October 4 2024

Contents

I History and presentation of my tutor and the laboratory 5

II Introduction and general description of the project 6

1 Electrical Network 7

2 Wind turbine production 8
2.1 Turbine and pitch control . . . 8
2.2 Generator . . . 11
2.2.1 Type VI . . . 12
2.3 Rectifier DC-Bus Voltage . . . 15

3 Grid Power control 15
3.1 LCL Filter . . . 15
3.2 Phase Locked Loop . . . 20
3.3 Grid Following . . . 20
3.4 Grid Forming . . . 21
3.4.1 Voltage Reference Generation . . . 23
3.4.2 Active power control . . . 25

III Simulation 28

4 Application to 480MW network 28
4.1 Network model . . . 28
4.2 Grid following . . . 28
4.3 Grid Forming . . . 30
4.3.1 Active power control of Virtual Synchronous Machine . . . 31
4.3.2 Active power control of PLL-Free . . . 33
4.4 Conclusion . . . 36

5 Effects of faults on 380MW network 36
5.1 List of faults . . . 36
5.2 Comparison of grid control strategy . . . 37
5.2.1 Three phases short circuit . . . 37
5.2.2 Injection Inverse Voltage . . . 40
5.2.3 Conclusion . . . 43

6 Digital twin of the wind power conversion 43
6.1 Development of the digital twin . . . 43
6.2 Grid-following Digital Twin . . . 44
6.3 Grid-forming Digital Twin . . . 45
6.3.1 Virtual Synchronous Machine Digital Twin . . . 45
6.3.2 Free-PLL Digital Twin . . . 47

6.4 Comparison between the real system and the digital twin during a short circuit. . . 48

IV Conclusion 50

V Appendix 51

A Virtual impedance code 51

B Current saturation 51

List of Figures

1 Aalto university campus . . . 5
2 Organisation chart for EEA common department of Aalto University . . . 6
3 Overview of the Finnish network . . . 7
4 Functional parameters for the model of the power coefficient for the 2 MW wind turbine. . . . 9
5 Model and measure of the power coefficient for 2MW wind turbine. The absolute error validates the high accuracy of the model . . . 9
6 Synoptic of the PI controller for adjusting the pitch angle of the turbine blades . . . 10
7 Synoptic of the PI controller for adjusting the pitch angle of the turbine blades . . . 10
8 Synoptic of the mechanical dynamic model of the turbine . . . 11
9 Exploded view of the Enercon wind turbine with direct driven type IV generator [5] . . . 12
10 Synoptic of the machine controller . . . 13
11 Synoptic of the dynamic model of the generator and its controller . . . 14
12 Representation of the DC bus, the inverter and the LCL filter . . . 15
13 Electric circuit of the capacitive filter with a passive statilizer circuit composed of a damped LC circuit . . . 16
14 Circuit representation of the transformer . . . 17
15 Bode diagram of the LCL filter transfer function . . . 19
16 Location of the LCL open loop poles in the complex plane . . . 19
17 Representation of the phase loop lock equipped with an anti-windup scheme. The proportional gain is set to k_p = 314.15 rad and the integral gain to $k_i = 2k_p$. . . . 20
18 Overview of Grid Following control strategy . . . 21
19 Synoptic of the dynamic model of the LCL filter and its controller . . . 21
20 VSC with a grid-forming control . . . 22
21 Overview of voltage reference generation [13] . . . 23
22 Generation of the reference voltage magnitude [13] . . . 24
23 Voltage and current control [13] . . . 24
24 Synoptic of frequency droop . . . 25
25 VSM-based grid-forming control . . . 25
26 IP-controller based active power control . . . 26
27 Grid model simscape . . . 28
28 Active and reactive power of Grid Following supplied at the turbine output connected to the network . . . 29

29 Grid frequency of Grid Following . . . 29
30 Grid current of Grid Following . . . 30
31 Output voltages of the voltage reference generation with quasi static power model . 30
32 DC bus controller . . . 31
33 Power reference . . . 31
34 Angle generation VSM . . . 32
35 Output voltages of the voltage reference generation VSM . . . 32
36 Active and reactive power of VSM supplied at the turbine output connected to the network with three phases fault . . . 33
37 VSM Grid frequency . . . 33
38 Angle generation Free PLL . . . 34
39 Output voltages of the voltage reference generation Free PLL . . . 34
40 Active and reactive power of Free PLL supplied at the turbine output connected to the network with three phases fault . . . 35
41 Free PLL Grid frequency . . . 35
42 Implementation of Three phases fault . . . 36
43 Implementation of injection of inverse voltage . . . 37
44 Frenquency of different control strategy during short circuit . . . 37
45 Grid following active and reactive power during short circuit . . . 38
46 free PLL active and reactive power during short circuit . . . 38
47 VSM active and reactive power during short circuit . . . 39
48 Complete system real with disturbance At 5.02 second. Transmission line powers,voltage and currents in case the wind . . . 39
49 Grid code and voltage grid measurements . . . 40
50 Frenquency of different control strategy during injection of inverse voltage . . . 41
51 Grid following active and reactive power during injection of $-1 \cdot 10^5$ . . . 41
52 Free PLL active and reactive power during injection of $-1 \cdot 10^5$ . . . 42
53 VSM active and reactive power during injection of $-1 \cdot 10^5$ . . . 42
54 Grid Power during faults . . . 43
55 Representation of the digital twin for modeling the wind farm from the turbine to the point of common coupling. . . . 44
56 Frequency response for grid-following digital twin . . . 45
57 Step response grid-following digital twin (Active and Reactive power) . . . 45
58 Frequency response for VSM digital twin . . . 46
59 Step response VSM digital twin (Active and Reactive power) . . . 46
60 Frequency response for Free-PLL digital twin . . . 47
61 Step response Free-PLL digital twin Active and Reactive power . . . 48
62 Frenquency of different digital-twin during short-circuit . . . 48
63 Grid following active and reactive power during short circuit . . . 49
64 free PLL active and reactive power during short circuit . . . 49
65 VSM active and reactive power during short circuit . . . 50

List of Tables

1 Parameters of the turbine and the pitch controller gains . . . 11
2 Parameters of the generator . . . 14
3 Parameters of the generator controllers . . . 14

4 Parameters of the LCL filter 18
5 Control parameters. 22
6 System parameters. 23

Part I
History and presentation of my tutor and the laboratory

My internship in Finland, from May to September, provided me with a valuable professional experience and a deep cultural immersion. Based in Helsinki, I was particularly struck by the city's rich architecture, blending classic influences and modernism. From Senate Square to buildings designed by Alvar Aalto, each edifice tells a story. I also explored Finland's diverse landscapes, from the Suomenlinna archipelago to the vast forests. Immersing myself in the Finnish way of life, particularly through the sauna tradition and the discovery of local cuisine, deepened my understanding of this society, which is deeply rooted in its heritage and nature. This stay allowed me to appreciate the work-life balance that characterizes the Finnish people.

Figure 1: Aalto university campus

During my internship at Aalto University, I had the opportunity to immerse myself in cutting-edge research at the Department of Electrical Engineering and Automation, specifically focusing on simulations of the electrical grid. Aalto University, formed in 2010 through the merger of three leading Finnish institutions—Helsinki University of Technology, the Helsinki School of Economics, and the University of Art and Design Helsinki—has quickly become a hub for interdisciplinary research and innovation in Europe.

The Department of Electrical Engineering and Automation, where my internship was based, is renowned for its advanced work in electrical engineering, control systems, automation, and robotics. Under the leadership of Professor Kyyrä Jorma, the department is committed to developing technologies that are both innovative and beneficial to society, particularly in areas like renewable energy and smart grids. You can find the simplified organization chart for my office Figure 2.

My internship was supervised by Floran Martin, an alumnus of my engineering school who now works as a researcher at Aalto. Floran guided me through the complexities of simulating electrical networks, helping me apply theoretical knowledge to practical scenarios. My work focused on improving and analyzing models for wind farms and their interaction with the Nordic electrical grid. Through this, I was able to enhance my understanding of how renewable energy sources integrate into large-scale electrical systems.

As part of the research team, I spent much of my time in an office shared by six colleagues working on diverse fields, such as engines, materials science, electromagnetics, and general electrical engi-

neering. The environment fostered collaboration and knowledge exchange, which was key to my development throughout the internship.
A significant part of my role as a researcher involved attending weekly project meetings held every Wednesday. During these meetings, team members presented their ongoing projects, exchanged feedback, and discussed recent advancements in their work. Researchers in the lab are primarily focused on writing scientific papers based on experimental and simulation data, as well as advancing knowledge in the field through collaboration and communication with peers in academia and industry.
Additionally, I gained experience in the typical responsibilities of a researcher, which include writing and publishing papers about the projects and experiments carried out in the lab. This process involves not only technical accuracy but also clear communication of the relevance and impact of the research findings on the scientific community and society as a whole.
Throughout my internship, I primarily focused on control strategies using MATLAB Simulink. Working alongside experts in the field, I was able to deepen my understanding of electrical grid simulations and gain practical experience in applying advanced modeling techniques, which will be invaluable for my future projects and career in electrical engineering.

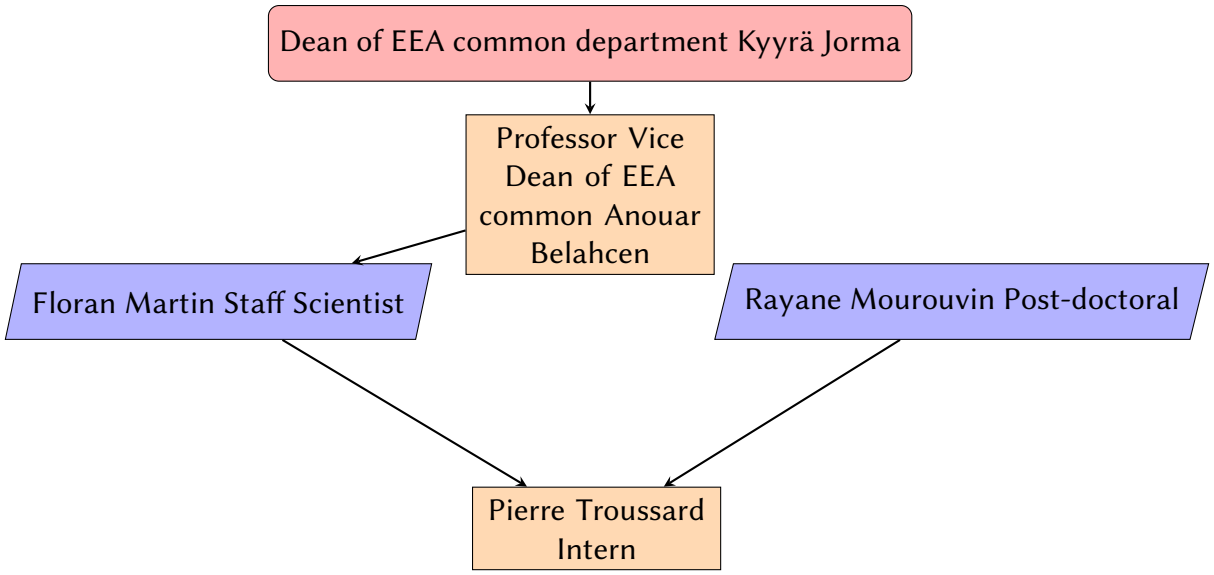

Figure 2: Organisation chart for EEA common department of Aalto University

Part II
Introduction and general description of the project

This internship report presents a wind farm model designed to represent the Nordic electrical grid. The model aims to capture the essential dynamics of wind turbines while remaining computationally efficient, meaning it enhances the model's speed without compromising accuracy. The analysis is demonstrated for a 2 MW wind turbine but can be extended to different generator capacities and topologies. Network control strategies, such as grid-following and grid-forming technologies, are

incorporated and studied.

First, I will define the theoretical aspects of this project, including the theoretical model of the turbine, the selected model for the electrical grid, and the different control topologies, namely one grid-following technology and two grid-forming technologies. The second part of this report will focus on implementing the different control strategies using Matlab software, based on the turbine model implemented by my supervisor, Floran Martin. Subsequently, robustness tests of the various control strategies will be carried out, compared, and analyzed under different network faults. The final part of this report will explore the implementation of a digital twin, allowing for much faster simulation of the turbine and control system. I will conduct additional robustness tests to ultimately conclude on the different strategies and control models for a wind turbine.

1 Electrical Network

Electricity networks are the essential infrastructure for distributing energy from generation sources to users, whether industrial, commercial or residential. A typical electricity network comprises generation plants, high-voltage transmission lines, transformer stations and distribution networks. The efficiency and stability of electricity networks are crucial to ensuring a continuous and reliable supply of energy, which is essential to the functioning of modern societies.

It is made up of several key elements: power plants, the main grid, high-voltage distribution networks, other distribution networks and a variety of electricity consumers. Finland is part of the Nordic synchronous area, which also includes Sweden, Norway and eastern Denmark. It is connected to Estonia and the Central European system via high-voltage direct current links. These connections are crucial for maintaining grid stability and enabling cross-border energy exchanges.

Finland's main grid is managed by Fingrid [2], the transmission system operator. This high-voltage grid links the main power plants, factories and regional distribution networks. Approximately 14,500 kilometres long, it includes more than 120 transformer stations. This vast network is essential both for the national distribution of electricity and for international energy trade, enabling Finland to import and export electricity as required.

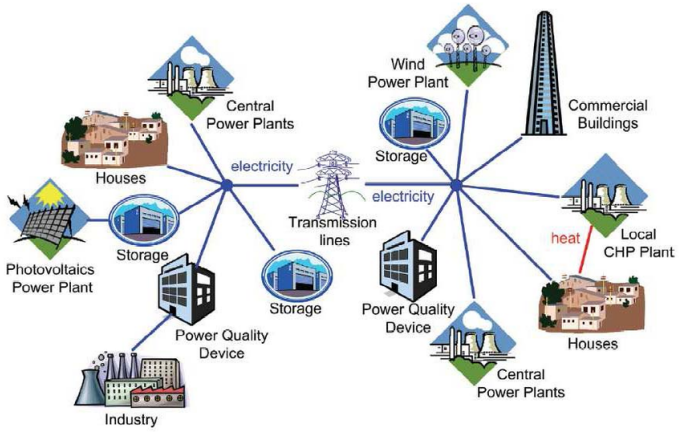

Figure 3: Overview of the Finnish network

Connected to the main grid, the distribution networks operate at voltages ranging from 0.4 kV to 110 kV. They ensure regional distribution of electricity and deliver it to a variety of end consumers, including households, industry, commercial buildings and farms. The majority of households are connected to low-voltage distribution networks, while large consumers, such as factories, can be connected directly to the main grid.

Finland's energy infrastructure is characterised by its diversity, incorporating nuclear, wind, solar and hydroelectric power. Nuclear energy plays a significant role, providing a stable and important share of the electricity produced in the country. Wind power is becoming increasingly important as Finland develops its renewable energy capacity.

2 Wind turbine production

In this section, I will describe the mathematical model of a wind turbine [1] [3] , focusing on the key components that influence its operation. The analysis includes the turbine and pitch control system, the generator, the rectifier, and the DC-bus voltage regulation. Each of these elements plays a crucial role in the efficient conversion of wind energy into electrical energy. By understanding the equations governing these components, we can optimize the performance and reliability of wind turbines in various operational conditions.

2.1 Turbine and pitch control

The orientation of the wind tower is assumed to face the wind direction. the yaw angle is properly controlled. The turbine rotating power can be calculated from the wind translational speed v_{wind}, the air density ρ_{air}, and the turbine radius R_{tur} :

$$P_{\text{wind}} = \frac{\rho_{\text{air}}}{2} \pi R_{\text{tur}}^2 C_p v_{\text{wind}}^3 \tag{1}$$

The power coefficient C_p depends on the pitch angle α of the blades and the factor λ that is the ratio between the blade tip speed and the wind speed

$$\lambda = \frac{R_{\text{tur}} \Omega}{v_{wind}} \tag{2}$$

with Ω , the turbine rotational speed.

Whereas the power coefficient Cp can be represented by a polynomial function of order 4, we would rather ensure the wind power to remain positive at low speed.

$$C_p = A \frac{\lambda^n \exp\left(-\frac{\lambda}{\lambda_0}\right)}{(\lambda_0 n)^n \exp\left(-n\right)} \tag{3}$$

with the model functional parameters A, n, and λ_0 that depend on the pitch angle α.
The measured power coefficient reported in [4] for a 2 MVA type IV wind turbine is used to identify the functional parameters of the model. The rotational speed is expressed as a function of the pitch angle of the turbine. It operates over the range -4° and +25°. One can see the evolution of the different functions in Figure 4.

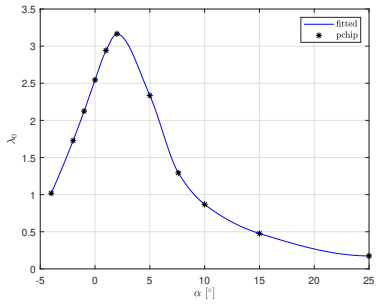

(a) Function A(α)

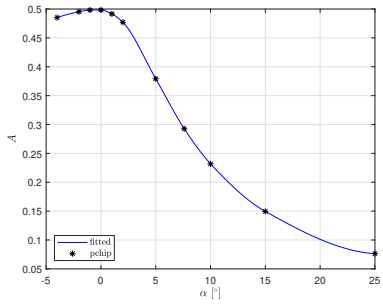

(b) Function n(α)

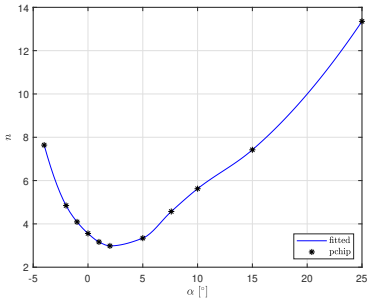

(c) Function $\lambda(\alpha)$

Figure 4: Functional parameters for the model of the power coefficient for the 2 MW wind turbine.

The model of the power coefficient of the turbine is depicted in Figure 5. This model accurately reproduces the measurements reported in [4], while also ensuring the physical requirement of a positive power coefficient. The highest error occurs at a pitch angle of $\alpha = -4°$ and a maximal tip speed ratio of $\lambda = 15$. It is important to note that the normal operation of the wind turbine typically occurs near the maximum point of the curve for any given pitch angle.

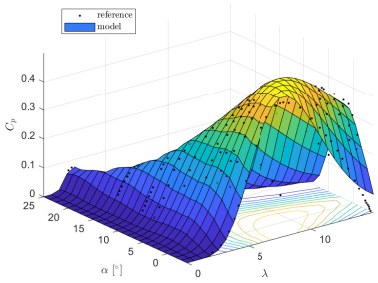

(a) Model and measure

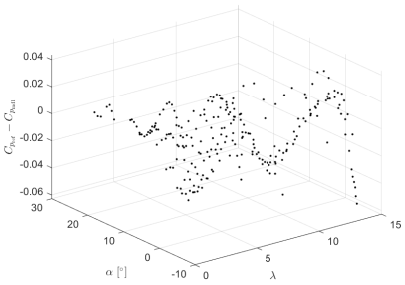

(b) Absolute error

Figure 5: Model and measure of the power coefficient for 2MW wind turbine. The absolute error validates the high accuracy of the model

The wind turbine is equipped with a pitch angle controller that aims to operate at the maximum power point of the power curve while respecting the mechanical limitations of the turbine. The pitch angle controller follows the reference indicated in Figure 6. The active power requirement starts when the wind speed reaches the cut-in speed $v_{\text{cut-in}}$. The maximum power tracking point of the pitch angles ensures a cubic evolution of the turbine power until the rated speed v_{rated}. Finally, the blades are inclined away from the wind direction to protect the turbine when dangerous speeds

higher than the cut-off speed $v_{\text{cut-off}}$ are reached. The turbine power reference remains zero for any wind speed exceeding $v_{\text{cut-off}}$.

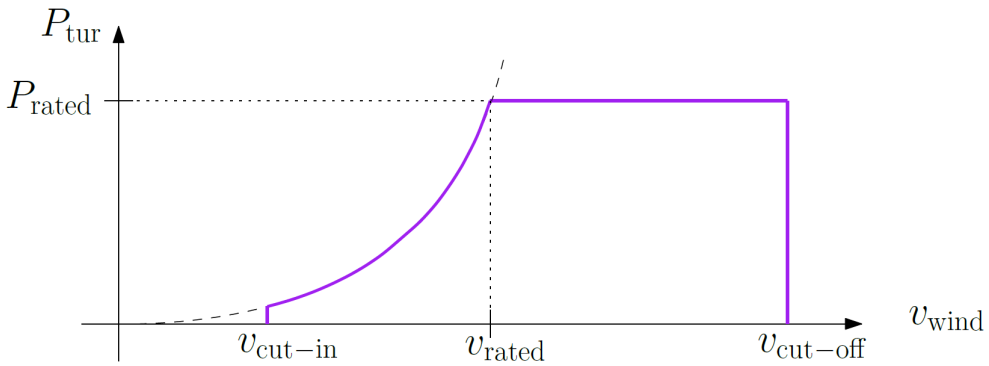

Figure 6: Synoptic of the PI controller for adjusting the pitch angle of the turbine blades

The pitch angle control is represented by the PI controller with the anti-windup topology represented in the Figure 7. The PI controller adjust the active power at the point of common coupling to the reference power that remains within the power envelop. The proportional action with parameter k_p adjust the pitch rate to reach the reference while the integral action with parameter k_i aims to reduce the static error. The saturation block ensure the controller pitch angle remains within the mechanical limitation. Finally, the anti-windup action with parameters k_{aw} improves the dynamic response by keeping the controller command to the limit when the saturation is activated. Usually, the anti-windup parameters is set to $1/k_p$ in order to ensure the controller response is at the saturation level.

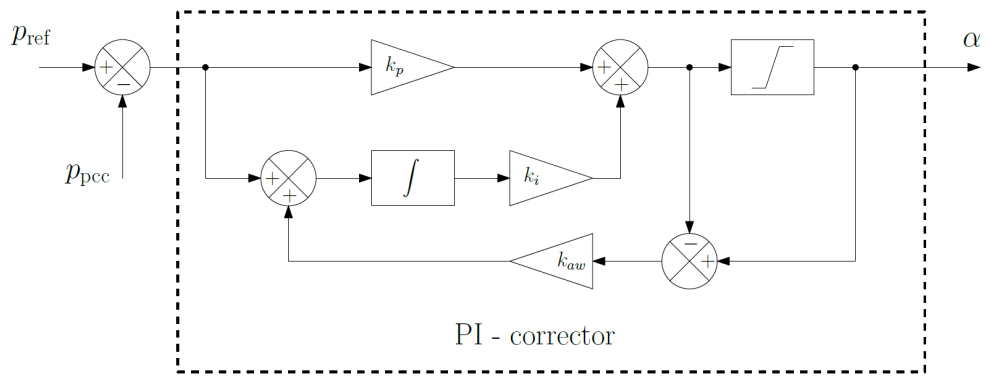

Figure 7: Synoptic of the PI controller for adjusting the pitch angle of the turbine blades

This classical structure of the PI corrector is kept for the rectifier control.

The dynamic model of the turbine is represented by the equation of rotational motion:

$$J_t \frac{d\Omega}{dt} + D_t \Omega = -\frac{P_{\text{wind}}}{\Omega} - T_{\text{emg}} \tag{4}$$

where J_t and D_t are the moment of inertia and the mechanical damping, respectively.
The negative sign appears in the turbine torque $\frac{P_{\text{wind}}}{\Omega}$ to adopt the generator convention for positive wind speed. The parameters of the 2 MW turbine are reported in the Table 1.

Parameter	Value
Air density, ρ_{air} [kg/m^3]	1.25
Rotor radius, R_{air} [m]	50
Nominal speed [rpm]	12
Cut-in speed [m/s]	3
Wind speed, Ω [m/s]	12
Cut-off speed [m/s]	25
Pitch gain, k_p [°/W]	$5 \cdot 10^{-6}$
Integral gain, k_i [°/J]	$5 \cdot 10^{-5}$
Anti-windup gain, k_{aw} [W/°]	$2 \cdot 10^{5}$
Rated power [W]	$2 \cdot 10^{6}$
Total inertia, J_t [kg m^2]	$2 \cdot 10^{6}$
Damping coefficient, D_t [Nm s/rad]	$13 \cdot 10^{3}$

Table 1: Parameters of the turbine and the pitch controller gains

The synoptic of the mechanical model of the turbine are represented in the Figure 8. The rotational speed of the turbine Ω is evaluated from the wind speed v_{wind}, the reference active power pref , and the electromagnetic torque of the generator T_{emg}. The power reference is ensured to remain within the power envelop depicted in Figure 6.

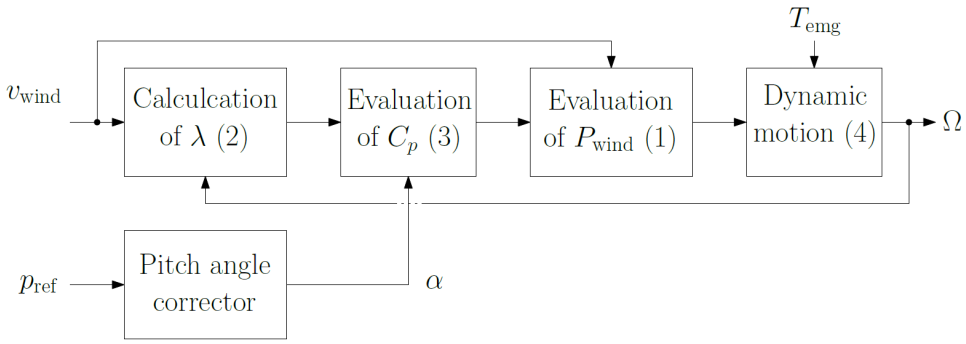

Figure 8: Synoptic of the mechanical dynamic model of the turbine

2.2 Generator

Nowadays, technological advancements allow for the improvement of wind turbine technology in terms of rated capacity and efficiency. The increase in rated capacity implies the increase in the height of the wind turbine and the diameter of its rotor. Depending on the wind turbine configuration, there are four types of wind turbines. The first two types correspond to older types of wind turbines, while the latter two types are the wind turbines currently being installed.

- **Type-I:** Fixed-speed wind turbine with a squirrel-cage induction generator (SCIG);
- **Type-II:** Partially variable-speed wind turbine with a wound rotor induction generator (WRIG);
- **Type-III:** Variable-speed wind turbine equipped with a doubly-fed induction generator (DFIG);
- **Type-IV:** Variable-speed wind turbine with a permanent magnet synchronous generator (PMSG).

The Type-IV wind turbine is commonly deployed for new WPP projects. In this type of wind turbine, the turbine rotor is connected to a PMSG which is then interfaced to the grid using a back-to-back

(B2B) converter. The B2B converter contains the machine-side converter (MSC) and the grid-side converter (GSC). The GSC can operate in both grid-following and grid-forming modes. Therefore, the special features of the transition between grid-following and grid-forming are relevant for a Type-IV wind turbine.

2.2.1 Type VI

The Enercon E82 2 MW is a type IV generator is a direct driven permanent magnet synchronous generator with damping bar [5] . It is represented in Figure 9. The control summary and grading check were carried out by my course supervisor. To do this we had to identify the engine equation.(the numerical values of the parameters used for this identification are shown in Table 2)

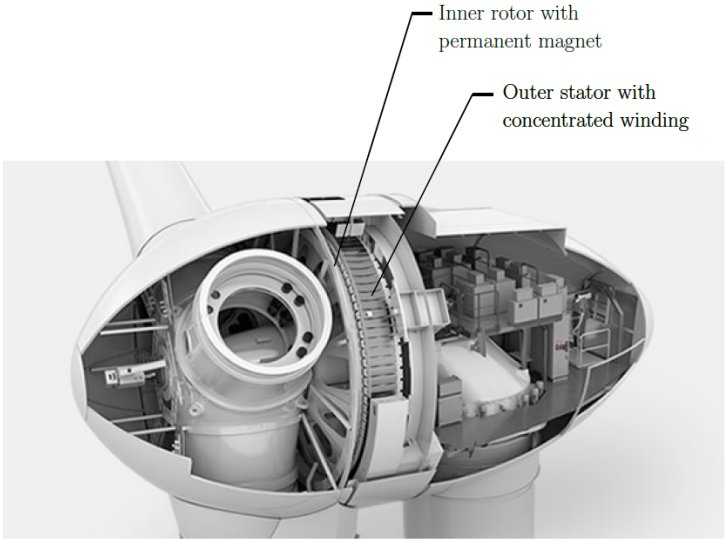

Figure 9: Exploded view of the Enercon wind turbine with direct driven type IVgenerator [5]

We therefore end up with the following state model present in [6]

$$\mathbf{x_m} = \begin{bmatrix} i_{dm} & i_{qm} & \psi_{kd} & \psi_{kq} \end{bmatrix}^T$$

$$\begin{cases} \frac{d\mathbf{x_m}}{dt} = \mathbf{A_m} \cdot \mathbf{x_m} + \mathbf{B_m} \cdot \mathbf{u_m} \\ \mathbf{y_m} = \mathbf{C_m} \cdot \mathbf{x_m} + \mathbf{D_m} \cdot \mathbf{u_m} \end{cases} \tag{5}$$

where $\mathbf{y_m} = \begin{bmatrix} i_{dm} & i_{qm} \end{bmatrix}^T$ is the vector of the measured signals.
The vector of inputs is $\mathbf{u_m} = \begin{bmatrix} v_{dm} & v_{qm} & \psi_{pm} \end{bmatrix}^T$.
The matrices are defined by:

$$\mathbf{A_m} = \mathbf{A_i}^{-1} \begin{bmatrix} -r_s & (L_q - \frac{L_{mq}^2}{L_{kq}})\omega & 0 & \frac{L_{mq}\omega}{L_{kq}} \\ -(L_d - \frac{L_{md}^2}{L_{kd}})\omega & -r_s & -\frac{L_{md}\omega}{L_{kd}} & 0 \\ \frac{L_{md}r_{kd}}{L_{kd}} & 0 & -\frac{r_{kd}}{L_{kd}} & 0 \\ 0 & \frac{L_{mq}r_{kq}}{L_{kq}} & 0 & -\frac{r_{kq}}{L_{kq}} \end{bmatrix} \tag{6}$$

$$\mathbf{B_m} = \mathbf{A_i}^{-1} \begin{bmatrix} 1 & 0 & 0 \\ 0 & 1 & -(1 - \frac{L_d}{L_{kd}})\omega \\ 0 & r_{kd}/L_{kd} & 0 \\ 0 & 0 & 0 \end{bmatrix} \tag{7}$$

With:

$$\mathbf{A_i} = \begin{bmatrix} L_d - \frac{L_{md}^2}{L_{kd}} & 0 & \frac{L_{md}}{L_{kd}} & 0 \\ 0 & L_q - \frac{L_{mq}^2}{L_{kq}} & 0 & \frac{L_{mq}}{L_{kq}} \\ 0 & 0 & 1 & 0 \\ 0 & 0 & 0 & 1 \end{bmatrix} \tag{8}$$

$$\mathbf{C_m} = \begin{bmatrix} 1 & 0 & 0 & 0 \\ 0 & 1 & 0 & 0 \end{bmatrix} \tag{9}$$

$$\mathbf{D_m} = \mathbf{0} \tag{10}$$

Thanks to the stator resistance and the damping bar, the open loop system is strictly stable, its poles have strictly negative real part. The active power at the point of coupling is controlled with the d axis current of the machine and the RMS voltage of the generator is controlled with the q axis current of the machine. The synoptic in the Figure 10 represents the control applied to the generator with the PI corrector structure already depicted in the Figure 7. The RMS voltage error is evaluated in order to ensure a negative reference of the q axis to apply an electromagnetic torque opposing the torque generated by the turbine. to the torque generated by the turbine.

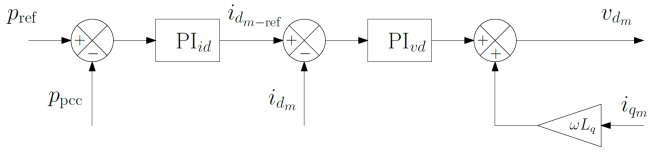

(a) Active power control via the d axis current of the machine

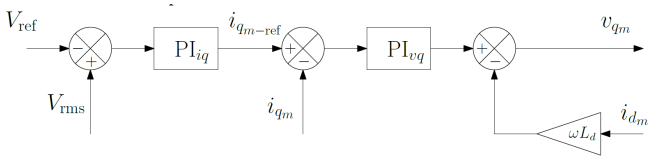

(b) RMS voltage of the generator control via the q axis current of the machine

Figure 10: Synoptic of the machine controller

The Figure 11 presents the synoptic of the generator with the controller. The active power controller is enables only when the RMS voltage of the machine reaches 90 % of its reference value. The active power reference should respect the power envelop depicted in Figure 6. The reference rms voltage v_{ref} should be set to the nominal RMS voltage of the generator Vm. The electric pulsation ω is deduced from the rotor speed Ω, an output of the mechanical dynamic system of the turbine (Figure 8). Furthermore, the output electromagnetic torque T_{emg} of the generator dynamic model is also connected to this mechanical block. The generator parameters are reported in the Table 2 and Table 3 .

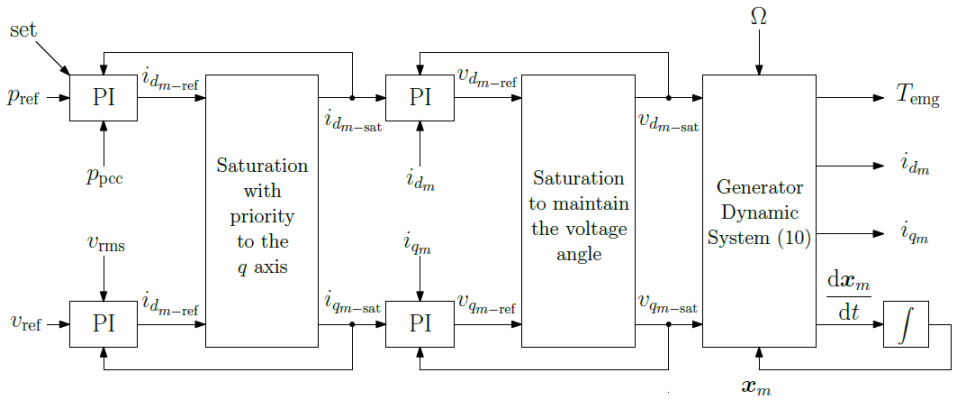

Figure 11: Synoptic of the dynamic model of the generator and its controller

Parameter	**Value**
Nominal RMS voltage, V_m	690 V
Nominal RMS current, I_m	1670 A
Stator resistance, r_s	0.4 mΩ
Rotor bar d-axis resistance, r_{kd}	13 mΩ
Rotor bar q-axis resistance, r_{kq}	43 mΩ
Stator d-axis inductance, L_d	0.7 mH
Stator q-axis inductance, L_q	1.4 mH
Permanent magnet flux, ψ_{pm}	2.98 Vs
Rotor bar d-axis inductance, L_{kd}	0.8 mH
Rotor bar q-axis inductance, L_{kq}	1.5 mH
Mutual d-axis inductance, L_{md}	0.6 mH
Mutual q-axis inductance, L_{mq}	1.3 mH
Stator leakage inductance, L_{ls}	46 μH

Table 2: Parameters of the generator

Controller	**Parameter Value**
Active power controller	
k_{ipd}	295 μA/W
$k_{i\omega d}$	47.3 mA/J
d current controller	
$k_{pv\omega d}$	238 mV/A
$k_{iv\omega d}$	11.9 V/(As)
RMS voltage controller	
$k_{i\omega q}$	4.2 A/s
$k_{pv\omega q}$	21 A/(Vs)
q current controller	
$k_{iv\omega q}$	238 mV/A
$k_{piv\omega q}$	23.8 V/(As)

Table 3: Parameters of the generator controllers

2.3 Rectifier DC-Bus Voltage

The DC bus voltage connects the current from the motor side i_{mot} to the grid side i_{lcl}. The dynamic model can be derived from the Equation 11:

$$C_{DC}\frac{dv_{DC}}{dt} = i_{lcl} - i_{gen} - \delta_{chop}\frac{v_{dc}}{R_{DC}} \tag{11}$$

The chopper activation is modeled with δ_{chop}. It activates if the voltage v_{DC} exceeds 1.05 the rated voltage V_{DC} = 1.45 kV then it is released when v_{DC} is lower than 0.95 of the rated DC voltage.

$$i_{gen} = \frac{I_{dq}^{mot}}{\sqrt{6}} \quad ; \quad i_{lcl} = \text{sign}(i_{di})\frac{I_{dq}^{lcl}}{\sqrt{6}} \tag{12}$$

with I_{dq}^{mot} and I_{dq}^{lcl}, the amplitude of the dq-axis current in the motor and the inverter side, respectively. The DC can be either discharged by the electric network when the inverter d-axis current i_{di} is negative or charged with positive current. The case of the wind turbine acting as a motor for sheding electric power would be considered by also considering the sign of the q-axis current of the generator which change the torque sign.

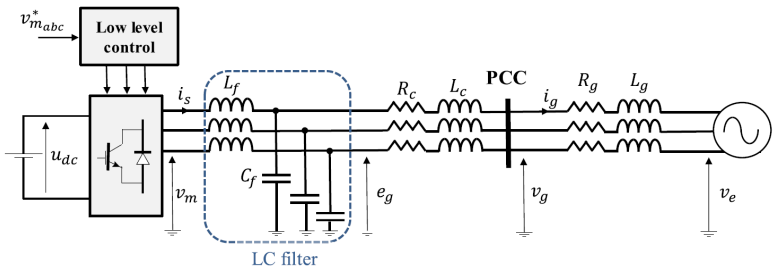

Figure 12: Representation of the DC bus, the inverter and the LCL filter

3 Grid Power control

3.1 LCL Filter

In this section we will look at how the LCL filter works in our system. LCL filters are low-pass filters that guarantee coupling between the various sources and provide good attenuation for frequencies above the system's cut-off frequency. In addition, it guarantees better coupling between the network impedance and the current through the network inductance. The synoptic of the LCL filter Figure 12 contains an inductance L_i on the inverter side, a capacitive bank with a passive stabilizer circuit, and a transformer to connect the medium voltage to the high voltage of the electrical grid. The leakage inductance L_g of the transformer can be considered as the grid side inductance to the point of common coupling. Its operation is defined in the following sub-sections.

Capacitive bank with passive stabilizer circuit

The capacitor C_f is equipped with a RLC circuit for damping the voltage ripples. The Figure 13 represents the electric circuit of the capacitive filter.

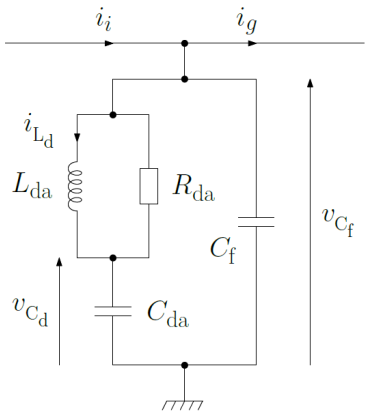

Figure 13: Electric circuit of the capacitive filter with a passive statilizer circuit composed of a damped LC circuit

The dynamic response of the capacitive circuit is modeled with the following differential equation set.

$$\begin{cases} C_f \frac{dv_{cf}}{dt} = i_u - i_a - i_{Ld} - \frac{(v_{cf} - v_{cd})}{R_{da}} \\ C_{da} \frac{dv_{cd}}{dt} = i_{Ld} + \frac{(v_{cf} - v_{cd})}{R_{da}} \\ L_{da} \frac{di_{Ld}}{dt} = v_{cf} - v_{cd} \end{cases} \tag{13}$$

Whereas a classical LCL filter present a resonance peak between the operating frequency and the switching frequency, the LC circuit is a trap filter which aims to attenuate the resonance peak [7]. Further damping reduction of the resonance peak can be attained by including a resistance in the trap filter [8].

Transformer

The transformer increases the voltage from the medium voltage to the high-voltage of the common coupling point. Due to the saturation of the magnetic circuit, the voltage spikes are filtered by the transformer. The transformer is represented by an electric circuit where the secondary inductance and resistance are projected in the primary side (Figure 14). The dynamic model of the transformer can be expressed by the following set of differential equations

$$\begin{cases} L_{11} \frac{di_g}{dt} &= v_{Cf} - R_1 i_g - R_\mu (i_g - i'_G - i_m) \\ L_{12} \frac{di'_G}{dt} &= R_\mu (i_g - i'_G - i_m) - R_2 i'_G - v'_g \\ L_m \frac{di_m}{dt} &= R_\mu (i_g - i'_G - i_m) \end{cases} \tag{14}$$

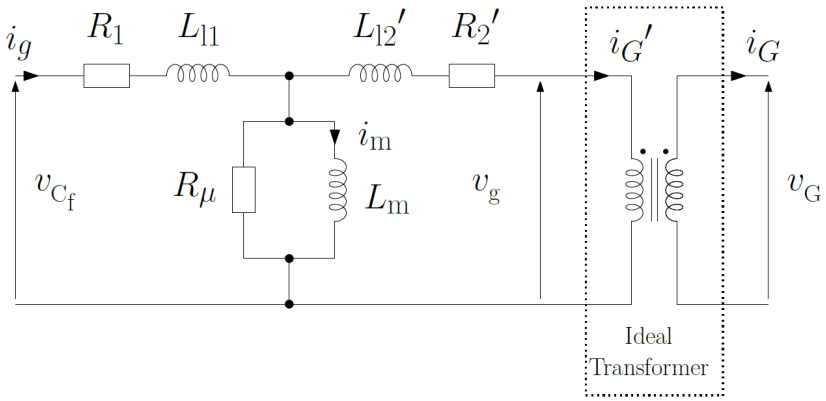

Figure 14: Circuit representation of the transformer

State-space representation

In order to derive a robust control of the grid active and reactive power, the LCL filter is represented in the grid dq-frame which is tracked by a phase loop locked. In practice, the magnetizing inductance is very small which requires a very small time-step. these very fast poles are the source of long simulations lasting around 30-40 minutes. Hence, in the rest of this document, the transformer is replaced by an equivalent inductance $L_g = L_{l1} + L'_{l2}$. Hence, the dynamic model of the LCL filter required the following remaining differential equation set.

$$\begin{cases} L_i \frac{di_i}{dt} = v_i - v_{Cf} \\ L_g \frac{di_g}{dt} = v_{Cf} - v_g \end{cases} \tag{15}$$

Together with the differential equations of the capacitive filter (Equation 13), the state-space representation of the LCL filter can take the matrix form

$$\begin{cases} \frac{dx_g}{dt} = A_g \cdot x_g + B_g \cdot u_g + B_{gp} \cdot W_g \\ y_g = C_g \cdot x_g + D_g \cdot u_g + D_{gp} \cdot w_g \end{cases} \tag{16}$$

dq-domain

The state-space variables contains the dq-axis of the inverter side current i_i, the voltage v_c across the filter capacity C_f , the voltage v_{cd} across the trap filter capacity C_{da}, the current i_l flowing through the trap filter inductance, and the grid side current i_g.

$$x_g = [i_{id}\ i_{iq}\ v_{cd}\ v_{cq}\ v_{cd_d}\ v_{cd_q}\ i_{ld_d}\ i_{ld_q}\ i_{g_d}\ i_{g_q}]^T \tag{17}$$

where the subscripts d and q indicate the components of the electrical quantities in the grid dq rotating frame. When performing the transformation from the phase quantities to the dq frame, the time derivative of the grid angle should not be omitted, as this term couples the dq electrical quantities.
The input quantities are the inverter voltages:

$$u_g = \begin{bmatrix} v_{id} \\ v_{iq} \end{bmatrix}.$$

The grid voltage can be considered as a perturbation of the system with:

$$w_g = \begin{bmatrix} v_{gd} \\ v_{gq} \end{bmatrix}.$$

The state-space matrices are:

$$\mathbf{A_g} = \begin{bmatrix} 0 & \omega_g & -\frac{1}{L_i} & 0 & 0 & 0 & 0 & 0 & 0 & 0 \\ -\omega_g & 0 & 0 & -\frac{1}{L_i} & 0 & 0 & 0 & 0 & 0 & 0 \\ \frac{1}{C_f} & 0 & -\frac{1}{C_f R_{da}} & \omega_g & \frac{1}{C_f R_{da}} & 0 & -\frac{1}{Cf} & 0 & -\frac{1}{Cf} & 0 \\ 0 & \frac{1}{Cf} & -\omega_g & -\frac{1}{CfR_{da}} & 0 & \frac{1}{CfR_{da}} & 0 & -\frac{1}{Cf} & 0 & -\frac{1}{Cf} \\ 0 & 0 & \frac{1}{C_{da}R_{da}} & 0 & -\frac{1}{C_{da}R_{da}} & \omega_g & \frac{1}{Cda} & 0 & 0 & 0 \\ 0 & 0 & 0 & \frac{1}{C_{da}R_{da}} & -\omega_g & -\frac{1}{C_{da}R_{da}} & 0 & \frac{1}{C_{da}} & 0 & 0 \\ 0 & 0 & \frac{1}{Lda} & 0 & -\frac{1}{Lda} & 0 & 0 & \omega_g & 0 & 0 \\ 0 & 0 & 0 & \frac{1}{Lda} & 0 & -\frac{1}{Lda} & -\omega_g & 0 & 0 & 0 \\ 0 & 0 & \frac{1}{L_g} & 0 & 0 & 0 & 0 & 0 & 0 & \omega_g \\ 0 & 0 & 0 & \frac{1}{Lg} & 0 & 0 & 0 & 0 & -\omega_g & 0 \end{bmatrix} \tag{18}$$

$$B_g = \begin{bmatrix} \frac{1}{L_i} & 0 \\ 0 & \frac{1}{L_i} \\ 0 & 0 \\ 0 & 0 \\ 0 & 0 \\ 0 & 0 \\ 0 & 0 \\ 0 & 0 \end{bmatrix} \quad \text{and} \quad B_{gp} = \begin{bmatrix} 0 & 0 \\ 0 & 0 \\ 0 & 0 \\ 0 & 0 \\ 0 & 0 \\ 0 & 0 \\ -\frac{1}{L_g} & 0 \\ 0 & -\frac{1}{L_g} \end{bmatrix} \tag{19}$$

The grid side current are measured so $y_g = \begin{bmatrix} i_{g_d} & i_{g_q} \end{bmatrix}^T$. Hence, we have

$$C_g = \begin{bmatrix} 0 & 0 & 0 & 0 & 0 & 0 & 1 & 0 \\ 0 & 0 & 0 & 0 & 0 & 0 & 0 & 1 \end{bmatrix} \tag{20}$$

with $D_g = 0$ and $D_{gp} = 0$. The passive damping circuit of the capacitive filter enables the possibility of the open-loop system to present poles with negative and nil real part. Hence, the open loop system is marginally stable. The inclusion of the resistance of the inductance winding leads to a completely stable open loop system.

Filter analysis

The parameters of the LCL filter are reported in the Table 4.

Parameter	**Value**
Nominal RMS voltage, V_g	690 V
Nominal RMS current, I_g	1670 A
Inverter inductance, L_i	335 µH
Grid inductance, L_g	1.1 mH
Filter capacitance, C_f	23.8 mF
Trap filter capacitance, C_{da}	700 µF
Trap filter inductance, L_{da}	621 µH
Trap filter resistance, R_{da}	1,33 Ω

Table 4: Parameters of the LCL filter

The transfer function of the filter is given with the Laplace variable s by [8]:

$$H(s) = \frac{i_g}{v_i} = \frac{L_{da}R_{da}C_{da}s^2 + L_{da}s + R_{da}}{D_5 s^5 + D_4 s^4 + D_3 s^3 + (L_i + L_g)L_{da}s^2 + (L_i + L_g)R_{da}s} \tag{21}$$

with $D_5 = L_i L_g L_{da} R_{da} C_{da} C_f$, $D_4 = L_i L_{da} L_g C_{da} + L_i L_g L_{da} C_f$,

$$and\ D_3 = (L_i L_g R_{da} C_{da} + L_i L_{da} R_{da} C_{da} + L_i L_g L_{da} C_f + L_g L_{da} R_{da} C_{da}).$$

The gain and the phase of the LCL filter are represented in the Bode diagram in Figure 15. The behaviour of the amplitude and the phase are comparable to the curve depicted in [7] and [8] where the resonance peak at 64.5 Hz is significantly damped by the resistance included in the trap filter. The stability is ensured until 100 Hz and the phase remains at -90°at 50 Hz and 60 Hz. Furthermore, the gain reaches 5.6 and 14.1 at 50 Hz and 60 Hz respectively. Since the the LCL gain is larger than ratio between the nominal current and the nominal voltage , the filter should be slightly over-sized for the operation at 50 Hz.

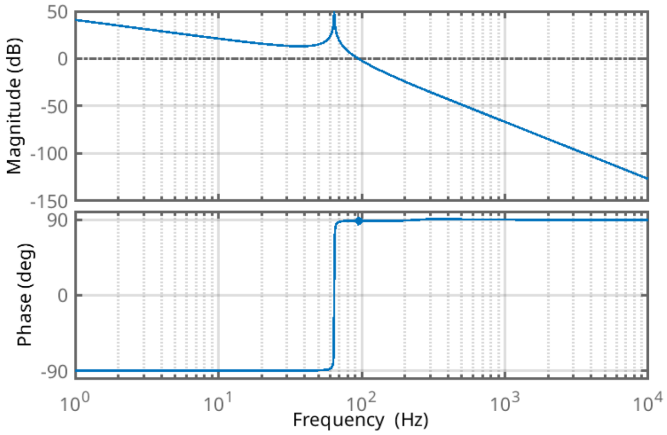

Figure 15: Bode diagram of the LCL filter transfer function

The eigenvalues of the matrix Ag contains the poles of the open-loop system. The 10 poles are represented in the Figure 16. There are 4 fast poles with negative real part which indicates the partial stability of the system and 6 poles located on the imaginary axis which involves a marginally stable system. Hence, the close loop system should be able to relocate these 6 poles in the stable region.

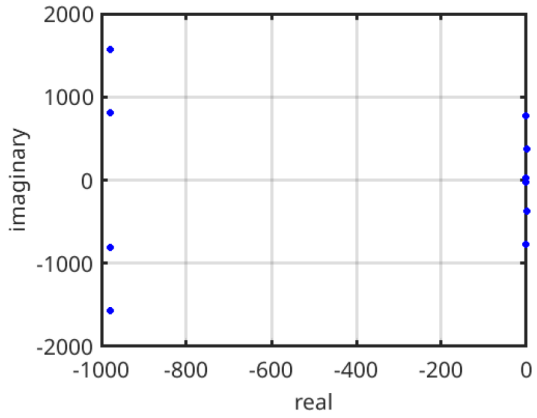

Figure 16: Location of the LCL open loop poles in the complex plane

In case the LCL filter needs to be redesigned, the reader can deploy the guidelines presented in [9] .

3.2 Phase Locked Loop

The Phase Locked Loop (PLL) applied in this case for tracking of the actual grid frequency [10]. The synoptic of the phase loop lock is represented in the Figure 17.

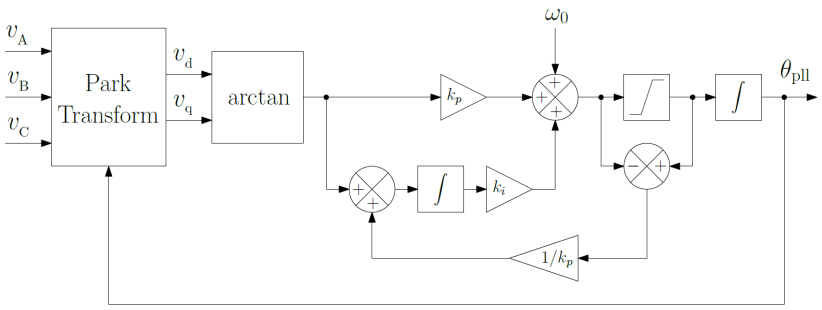

Figure 17: Representation of the phase loop lock equipped with an anti-windup scheme. The proportional gain is set to k_p = 314.15 rad and the integral gain to $k_i = 2k_p$.

This PLL is using first order low-pass filters on the estimated d- and q-axis voltage components and an inverse tangent function to calculate the phase angle error of the PLL. This phase angle error $ePLL$ is the input to a PI controller tracking the frequency of the measured voltage. For the practical implementation, the estimated frequency ωPLL is then integrated to obtain the estimate of the actual instantaneous phase angle δPLL used for transformation of the voltage measurements.

3.3 Grid Following

The network monitoring strategy controls the DC bus voltage with the d-axis axis, the network current igd and the network reactive power with the q axis igq . The purpose of controlling the network current is to ensure that the current and voltage remain within their limits. Since the open loop LCL system. Since the open loop LCL system contains marginally stable zeros and poles, the grid current controller is based on full state feedback. Although it is necessary to evaluate each state variable xg, it can be developed with a state-space observer with a limited number of state variables. Given that our project aims to develop a digital twin of the wind farm, the development of such a fast pole observer is not necessary.

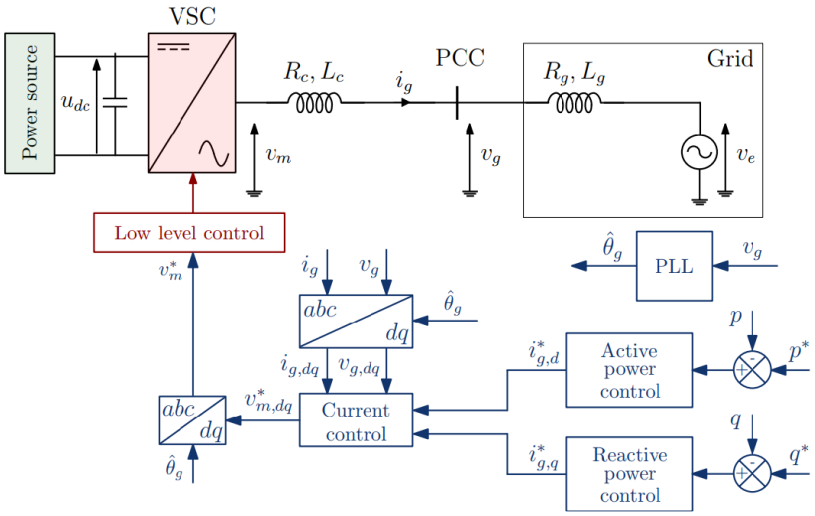

Figure 18: Overview of Grid Following control strategy

For current and voltage control, a control strategy based on state feedback control has been developed [11] and the linear quadratic regulator [12]. The improved controller offers several advantages over the classic PI control with anti-windup. The LQR method optimizes the controller gain, ensuring the system's state variables follow the best possible paths while keeping grid and inverter currents and voltages within safe limits. The full state feedback control strengthens the system's stability by precisely adjusting the system's poles, supported by an observer to manage noisy variables. This combination helps keep the filter capacitor voltage within acceptable limits and ensures the currents in the inductors stay within their physical limits.

The synoptic of the grid following controller is represented in the Figure 19.

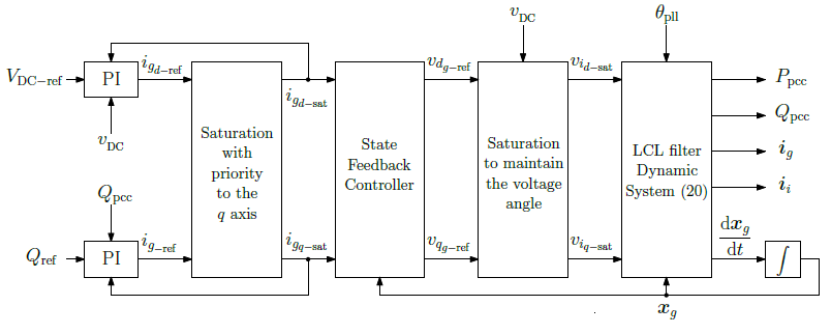

Figure 19: Synoptic of the dynamic model of the LCL filter and its controller

The dq axis reference are synchronized to the grid voltage thanks to the phase loop locked angle θ_{pll}. The inverter current i_i are fed to the DC bus subsystem which provides the limit voltage v_{DC} to the saturation block of the LCL inverter and the generator rectifier. The maximum modulation index of the space vector modulation can also be considered in the evaluation of the maximal available voltage.

3.4 Grid Forming

The **grid forming** technique acts as a voltage source, in contrast to **grid following**, which acts as a current source. In contrast to grid following, there is no need for LQR or state feedback to form

the grid; PI controllers for current, voltage, and active power control are sufficient.
In this section, we will study the implementation of the grid forming strategy, which is divided into two parts:

- **Voltage Reference Generation**: This step involves generating the voltage command in the dq domain. This part is common to most grid forming technologies.
- **Voltage Angle Generation**, commonly referred to as **active power control**: This angle provides the reference needed to transform the dq domain voltages to abc and vice versa, using the Park transformation.

I will present the implementation of two technologies for generating these angles. Firstly, the most common, is called **Virtual Synchronous Machine (VSM)**. This technology aims to emulate the behavior of a traditional synchronous generator using electronic converters. Secondly, known as **PLL-free Grid-Forming**, is noteworthy because, as its name suggests, it does not use a Phase-Locked Loop (PLL).

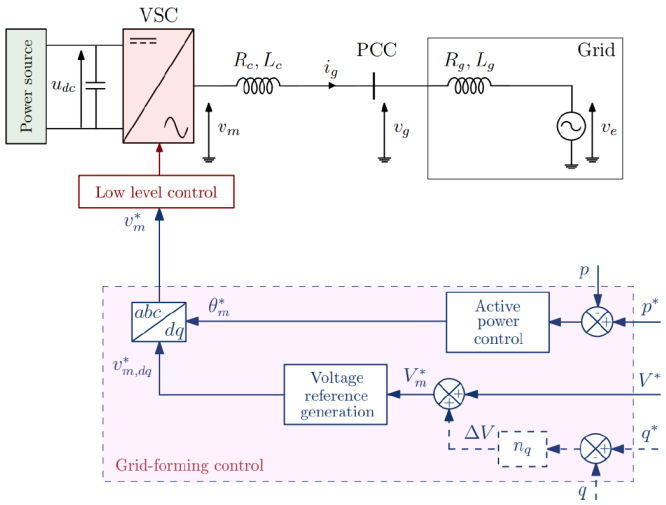

Figure 20: VSC with a grid-forming control

The useful parameter are given in the Table 5 below.

Control parameter	**Value**
Inertia constant, H	5 s
Proportional current gain, k_{pi}	3.0666 V/A
Proportional power gain, k_p	0.02 µrad/Ws
Integral current gain, k_{ii}	4.9989 V/A
Proportional voltage gain, k_{pv}	2.1844 A/V
Filter frequency of Reactive Power, ω_f	60 rad/s
Integral voltage gain, k_{iv}	4.8729 A/V
System constant, K	1200 Ws/rad

Table 5: Control parameters.

Parameter	Value
Nominal power, $P_{n1} = S_{b1}$	2 MW
Nominal frequency, f_n	50 Hz
Power factor, $\cos\phi$	1
AC voltage, U_{ac}	15.75 kV
Maximum DC current, $I_{\max SAT}$	3.6232 kA
Maximum AC current, $I_{\max VI}$	2.8986 kA
DC voltage, U_{dc}	1450 V
Stator reference voltage, e^*_{gdq0}	690 V
Stator voltage, e^*_{gq0}	0 V
Base DC impedance, Z_{basedc}	0.2381 Ω
Base AC impedance, Z_{baseac}	124.0312 Ω
Base angular speed, ω_b	314.1593 rad/s
Reactance-to-resistance ratio, $\sigma X/R$	5
q-axis damping coefficient, n_q	10^{-3}
q-axis proportional gain, k_{pRVI}	0.1588
Capacitance, C_f	23.8 mF
Resistance, R_v	0.0214 Ω
Filter inductance, $L_f = L_i$	335 µH

Table 6: System parameters.

3.4.1 Voltage Reference Generation

In accordance with [3] and [13], I will present the different parts of the voltage reference generation.

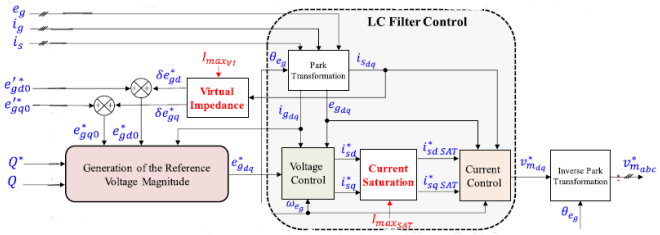

Figure 21: Overview of voltage reference generation [13]

Generation of the reference voltage magnitude.
The voltage reference generation section allows us to generate voltages in the dq domain according to the voltage setpoints, which are 690V for the d-axis and 0V for the q-axis. However, since this block depends on the dynamics of the current i_{gdq} delivered by the LCL filter, it is possible to observe oscillations at its output. Additionally, this block has a reactive power compensation function, but this is not effectively controlled in the grid forming control strategy.

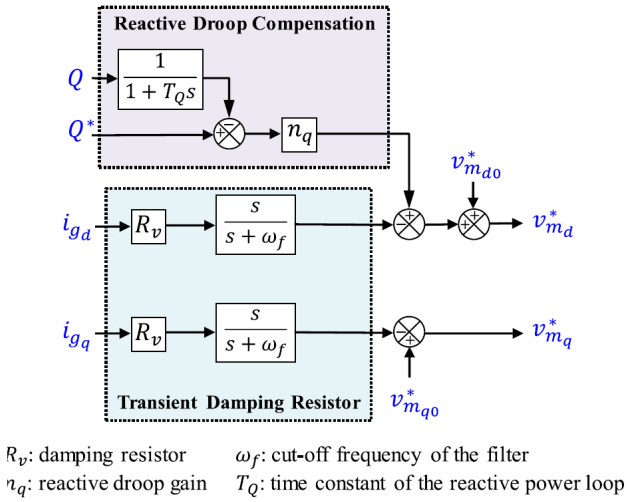

Figure 22: Generation of the reference voltage magnitude [13]

Virtual impedance

This Virtual Impedance is useful only when the input current exceeds the nominal current, which in our case is 2.8986 kA. It will therefore be useful during faults to restore the reference current and thus prevent the degradation of components.You could find the Matlab code of the virtual impedance in Appendix A.

Voltage and current control

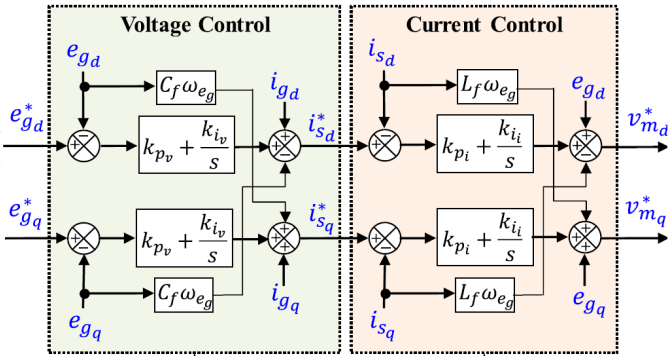

Figure 23: Voltage and current control [13]

After generating the voltages v_{dq} and injecting the angles δv_{md} and δv_{mq} from virtual impedance, an inverse PI controller in the current control loop is used to generate reference currents. These currents then pass through the current saturation algorithm proposed in Appendix B, and finally, another PI current controller is used to generate the final control voltage v_{mdq} for our grid forming the values of the coefficients kp ki are given in pu in the article [13] but in our case of 2 MW turbine all the important coefficients will be given in the Table 5 and Table 6 . Additionally, there is an action to compensate for the electromotive force using the product of the angular frequency generated by the active power control, the impedance of the capacitor from the LCL filter, and the grid voltages v_{gdq}. Similarly, the currents i_{sdq} are compensated with the inductance L_f of the LCL filter in our case calls L_i.

Current saturation
You could find the Matlab code of the current saturation in Appendix B.

3.4.2 Active power control

In the grid-forming control strategy, the active power control is one of the most crucial components. It allows us to generate the reference angle necessary for transforming quantities like currents and voltages between the dq and abc domains, and vice versa, ensuring synchronization with the grid frequency to ensure synchronisation with the grid frequency, the most important parameter for achieving this synchronisation is the value of the inertia of the Finnish grid, which you can find on the Fingrid [2] website and in the Table 5 and Table 6. Additionally, these functions are essential for controlling active power with stability, speed, and ensuring zero steady-state error.

It should be noted that the power reference P^* is not directly 2 MW. A frequency droop [15] was implemented Figure 24, characterized by the droop constant k_ω, which acts on the difference between a reference frequency ω_{M}^* and the actual speed ω_{m}. Finally, the reference power is given by the sum of the output of the k_ω block and the reference power p^*.

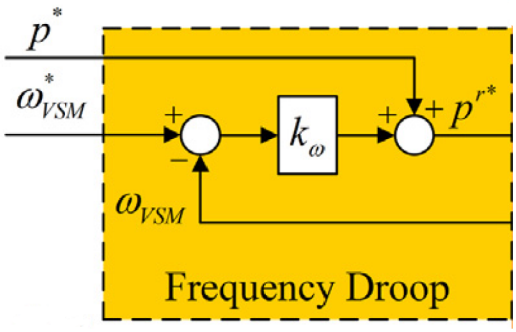

Figure 24: Synoptic of frequency droop

Virtual Synchronous Machine
The VSM active power control aims to replicate the behavior of a synchronous machine, particularly its characteristics like inertia response and natural damping you can see in the Figure 25 the block diagram of the VSM. The equations governing the scheme are given by the swing equations, which can be found, in the article [14].

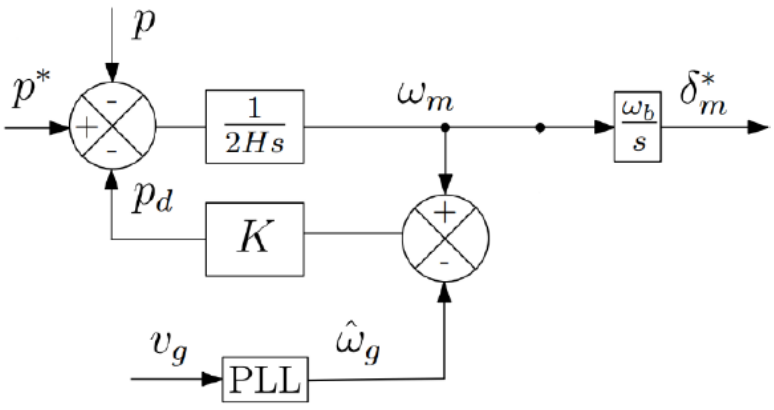

Figure 25: VSM-based grid-forming control

Moreover, the differential equation can be expressed as:

$$2H\frac{d\omega_m}{dt} = p^* - p - K(\omega_m - \hat{\omega}_g) \tag{22}$$

where p is the measured power, p^* is the power reference, p_d is the damping power, H is the inertia constant, K is the damping constant, ω_{set} is the frequency reference, and R_d is the frequency droop gain. This grid-forming control uses a PLL to decouple the inertia response and frequency support. In addition, you can find the complete implementation of the VSM in the Article [15].

Free PLL

PLL-free is another grid-forming technique analogous to VSM. The positive aspect of this strategy is absence of PLL and as a consequence lower sensitivity to network faults. This technique is represented by the block diagram shown in Figure 26. It consists of a specific formulation of the PI controller called the IP controller [13] and an integrator to generate the reference angle.

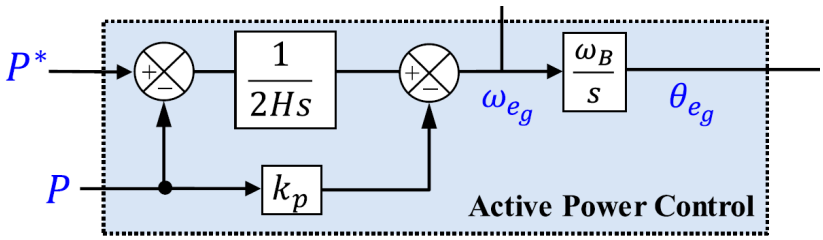

Figure 26: IP-controller based active power control

The relationship between the frequency, ω_m, and the active power for the IP controller is given by:

$$\omega_m = \frac{1}{2H}(p^* - p) - k_p p \tag{23}$$

To express the power in terms of angular frequencies, the equation can be rewritten as:

$$p = K_c\frac{(\omega_m - \omega_g)\omega_b}{s} \tag{24}$$

where $K_c = \frac{V_m V_e}{x_c + x_g}$, V_m and V_e are the magnitudes of the voltage, x_c and x_g are the reactances of the grid **(quasi static model)**, and ω_b is the base angular frequency.
Substituting this into the frequency expression, we get:

$$\omega_m = \frac{1}{2H}(p^* - p) - k_p K_c\frac{(\omega_m - \omega_g)\omega_b}{s} \tag{25}$$

This equation can be further simplified to:

$$2H\frac{d\omega_m}{dt} = (p^* - p) - 2Hk_p K_c(\omega_m - \omega_g)\omega_b \tag{26}$$

This formulation is similar to the angular frequency expression used in Virtual Synchronous Machines (VSM). However, the damping constant K in this context is defined as:

$$K = 2Hk_p K_c\omega_b \tag{27}$$

Assuming $V_m = V_e = 1$ p.u., the power transfer for the IP-controlled active power regulation is expressed as second order transfer function:

$$\frac{p}{p^*} = \frac{1}{\frac{2HK_c(\omega_b+s)}{\omega_b} + 2Hk_ps + 1} \tag{28}$$

The damping gain k_p is selected based on the desired damping ratio ξ and is calculated as:

$$k_p = \xi\sqrt{\frac{2(H(x_c + x_g)}{\omega_b}} \tag{29}$$

Finally, the natural frequency ω_n for the active power control is expressed as:

$$\omega_n = \frac{\omega_b}{\sqrt{2H(x_c + x_g)}} \tag{30}$$

By appropriately choosing ξ, ω_n, k_p, and H, the system can achieve the desired frequency support and inertia effects without needing a PLL.

Part III
Simulation

4 Application to 480MW network

The aim of these simulations is to validate the grid forming and grid following control strategies connected to a grid.

4.1 Network model

The grid model in Simscape was supplied to me by the network department. Figure 27, which is made up of three Controlled Voltage Sources directly connected to the source, in this case our turbine controlled either in grid forming or in grid following, the difference being that the grid following control is imaged as a current source, so we need to connect a resistor in parallel with our controlled voltage source and conversely our grid forming strategy is considered as a voltage source, so we need to connect a resistor in series with the controlled voltage source [16] . Then we have a three-phase messaging block that allows us to recover the voltages and currents at the point of common coupling, which allows us to send the values back to the controller via a PLL for grid following and just a park transformer for grid following thanks to our angle calculated in the Active power control section. Then we have a transformer and the inductance of the lines leading to our load, which could represent a factory, for example. Finally we find the image of the other Finnish power sources.

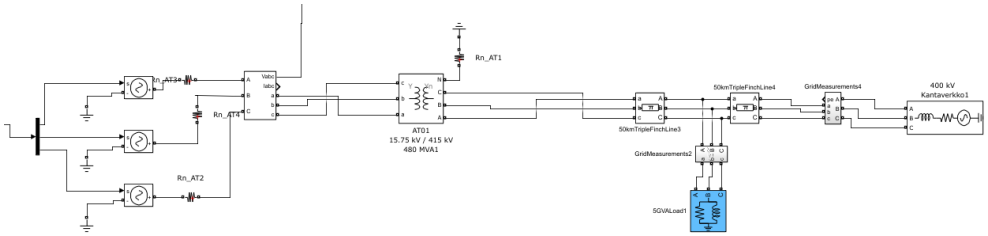

Figure 27: Grid model simscape

4.2 Grid following

After completing the literature review and familiarizing myself with the necessary tools, one of the first practical tasks of my internship was to connect the turbine, controlled by the network monitoring strategy, to the network supplied by the network department. This control strategy aims to regulate the active power to reach 2 MW while keeping the reactive power at zero during normal operation.
As shown in Figure 28, the system takes about 4 seconds to stabilize the reactive power and 10 seconds for the active power. The system is stable in normal operation, with no static errors.

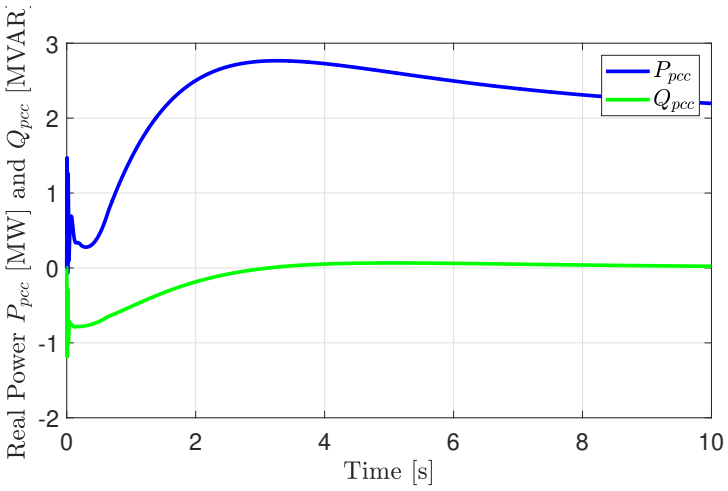

Figure 28: Active and reactive power of Grid Following supplied at the turbine output connected to the network

We can see in Figure 29 that the frequency is stable at 50Hz with a small spike on activation and remains stable.

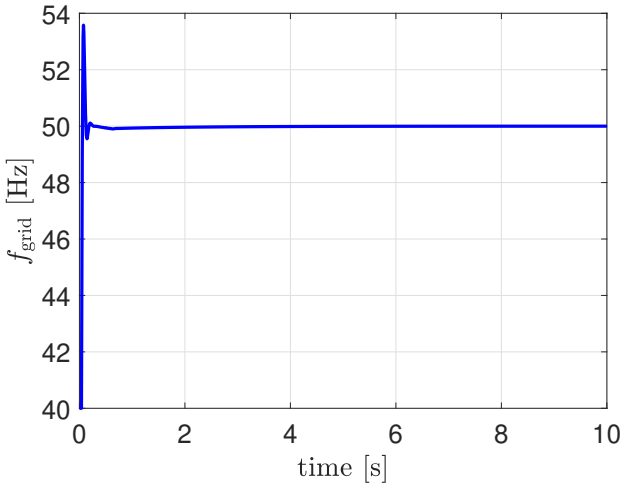

Figure 29: Grid frequency of Grid Following

As mentioned previously, the grid following strategy is imaged as a current source, that's why it is important to read the grid currents to validate the correct operation of the control. In Figure 30 we observe the dq currents with a response time of about 4s the q axis current is zero in agreement with our reactive power.

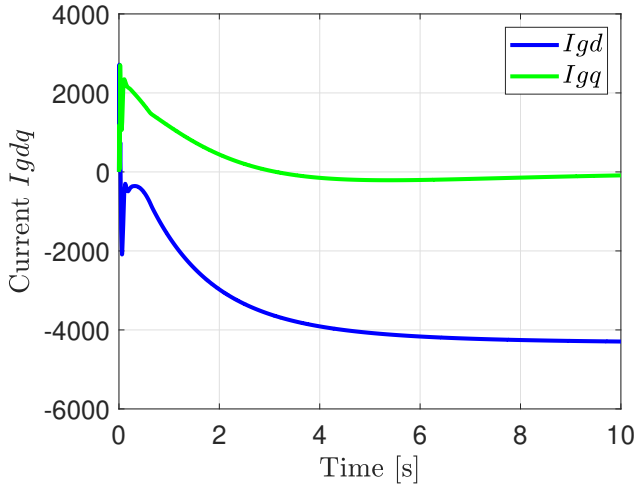

Figure 30: Grid current of Grid Following

4.3 Grid Forming

Based on the previous steps, after implemention my two grid-forming strategies, I used a quasi-static model of the active power and applied a step input for the power reference to validate my controller coefficients. This allowed me to observe the angles generated by the active power control, as shown in Figure 34 and Figure 38, and the two-phase output voltages from the voltage reference generation, as illustrated in Figure 31. The results align with our expectations, showing zero voltage on the q-axis and 690 V on the d-axis, consistent with the specifications.

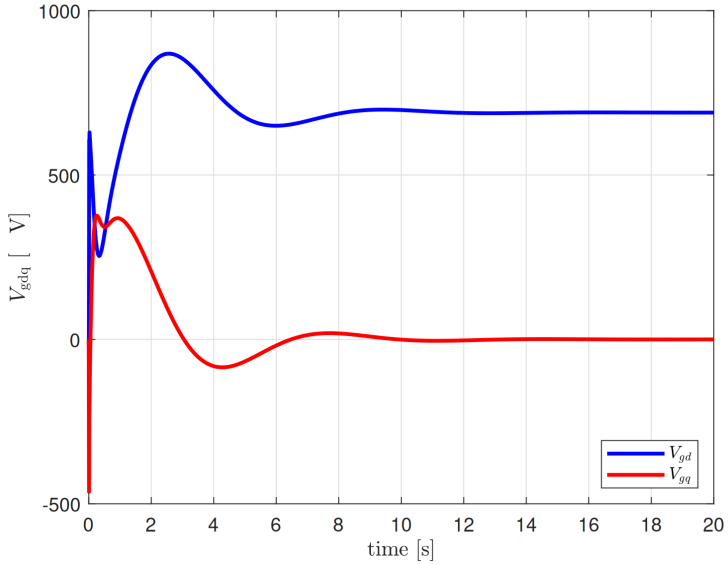

Figure 31: Output voltages of the voltage reference generation with quasi static power model

Then I made a controller [3] to control the voltage supplied by the DC bus shown in Figure 32 to be able to connect the complete turbine with a good power reference, the assembly is then connected to the grid.You can therefore see in Figure 33 the power reference coming from the dc bus,at around 0.5 you can see a spike, due to the load on the DC bus .

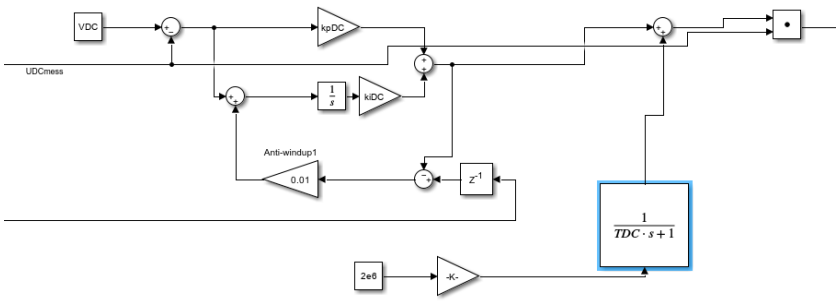

Figure 32: DC bus controller

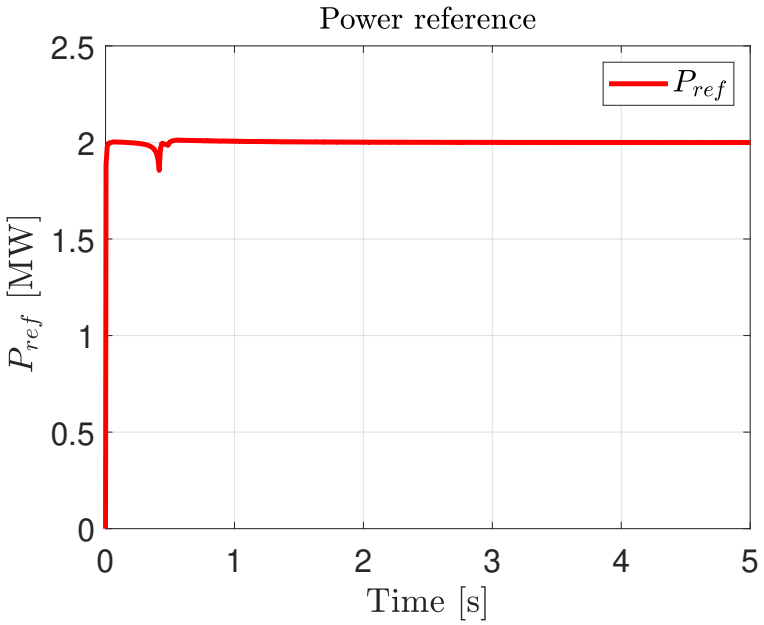

Figure 33: Power reference

4.3.1 Active power control of Virtual Synchronous Machine

We will be able to observe that in practice, with a complete grid and not a quasi-static model calculation, the values can differ. The generation of the grid angle by the VSm active power control in Figure 34 corresponds to the expectation, but we can see in Figure 35 the biphaser voltages which differ from the quasi-static system with a higher voltage for the d axis and a non-zero voltage, here these differences are due to the reactive power compensation shown in Figure 22.

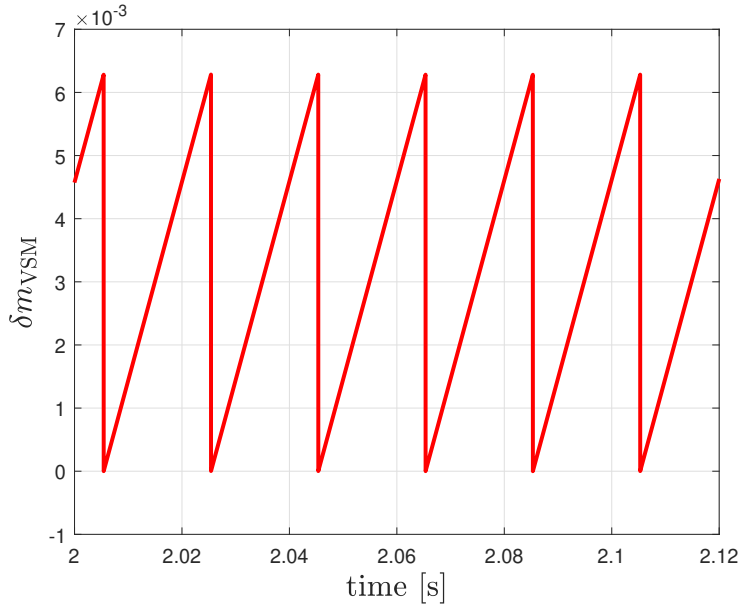

Figure 34: Angle generation VSM

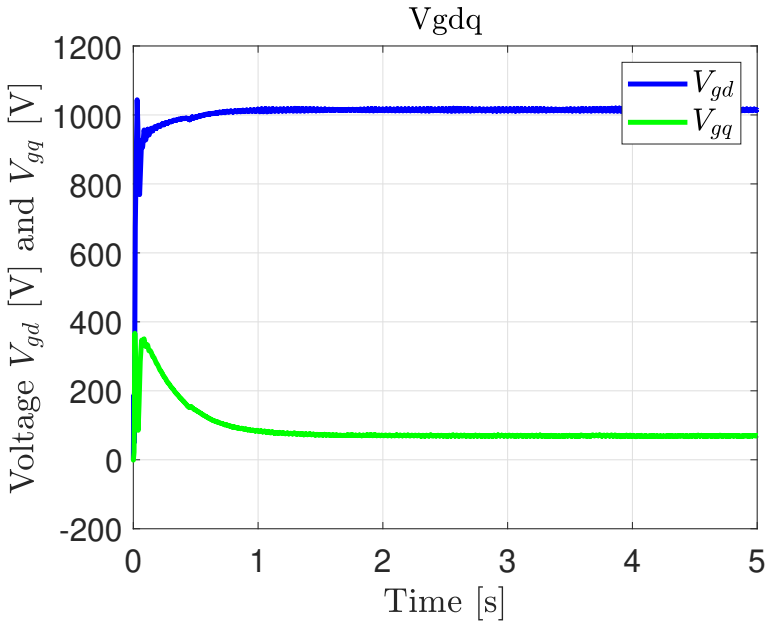

Figure 35: Output voltages of the voltage reference generation VSM

All that remains is to calculate our active and reactive powers at the point of common coupling using grid currents and voltages measurements. One can observe the responses of the active and reactive powers in Figure 36. We achieve a response time much faster than that of grid following, with a good active power value of 2 MW and no static error. As explained earlier, power is not controlled in grid forming, which is why it is not zero due to reactive droop compensation represented Figure 22, which does not completely reject reactive power.

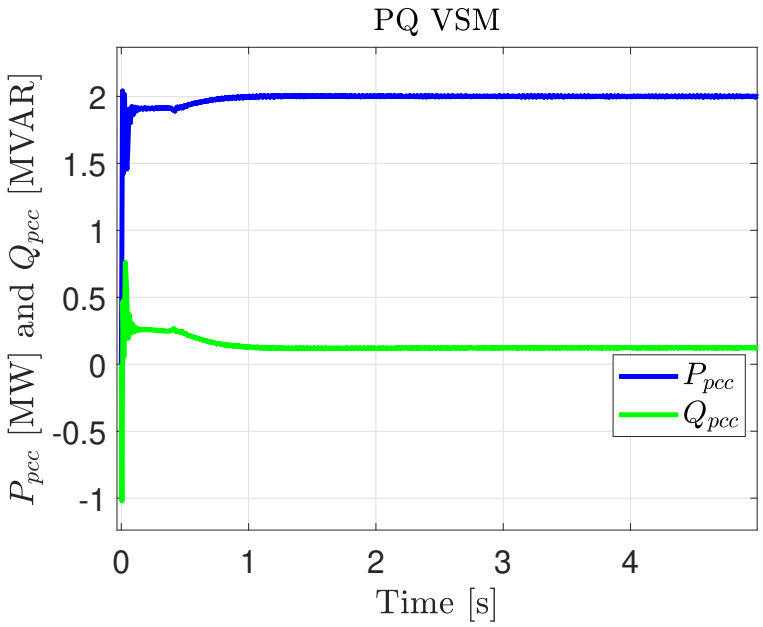

Figure 36: Active and reactive power of VSM supplied at the turbine output connected to the network with three phases fault

In Figure 37, one can observe the frequency from the point of common coupling. One can see that the grid frequency of 50 Hz is in line with the specifications, with a little noise.

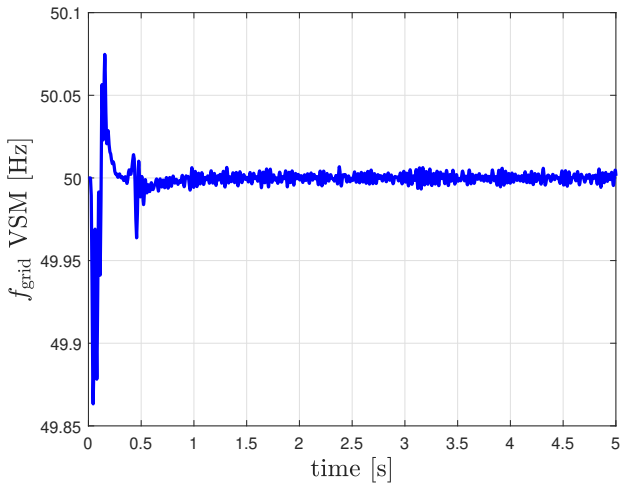

Figure 37: VSM Grid frequency

4.3.2 Active power control of PLL-Free

In accordance with the VSM strategy, which is analogous to a free PLL, we can observe that the angle generated by the active power control, Figure 38.

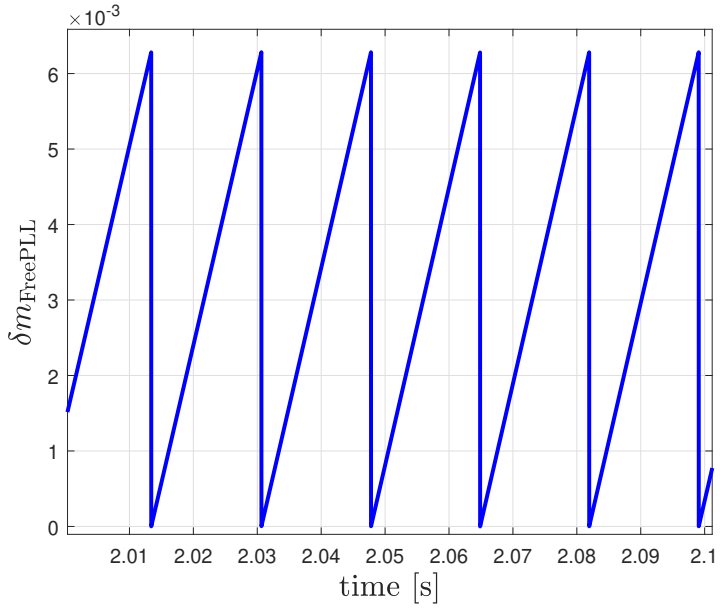

Figure 38: Angle generation Free PLL

the results of the two-phase voltages of the complete simulation are satisfactory and give us a zero d-axis and the d-axis is almost at 690V due to the reactive power compensation.

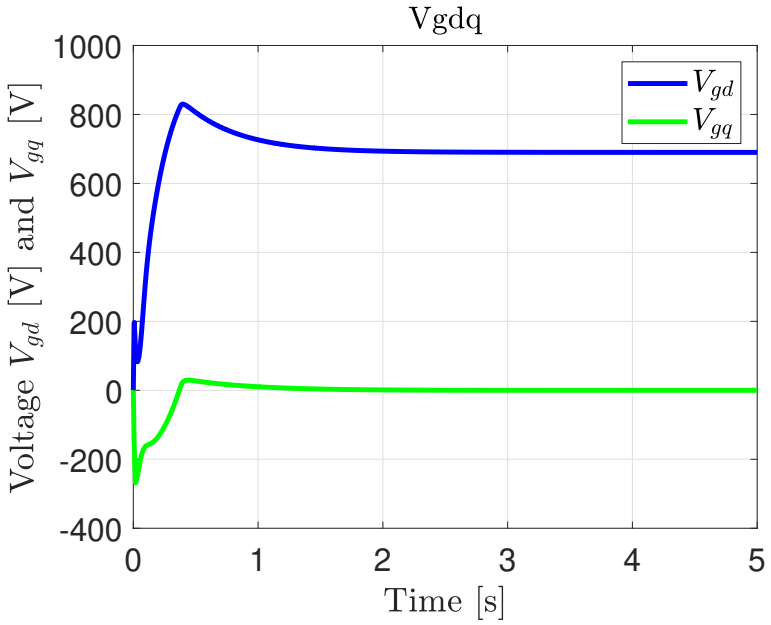

Figure 39: Output voltages of the voltage reference generation Free PLL

The active power response in Figure 40 is in good agreement with a first or 2nd order transfer function described in Equation 28 with a very fast response time and with 2MW in final value in agreement with the specification. In addition, we can see that the reactive power compensation does its job well but the final value is not zero.

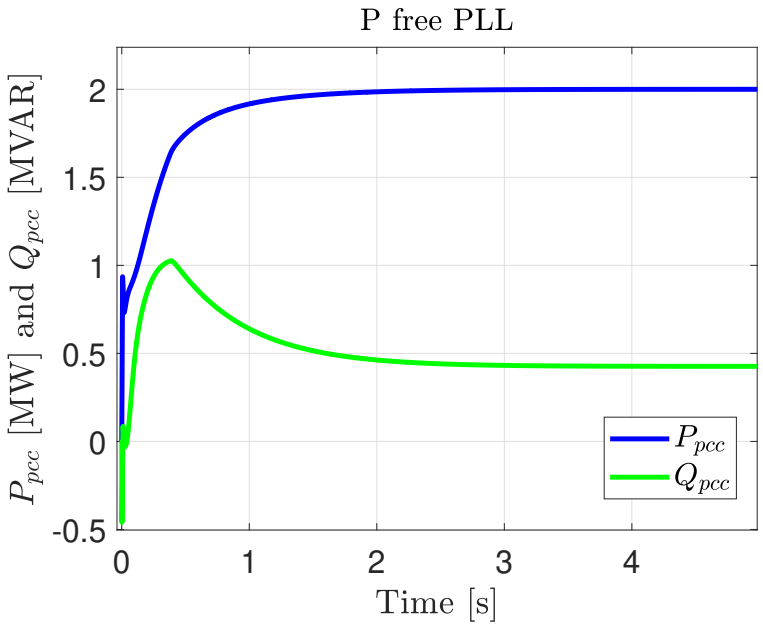

Figure 40: Active and reactive power of Free PLL supplied at the turbine output connected to the network with three phases fault

The frequency response at the PCC is also well-tuned to 50 Hz. Noise-free even without pll.

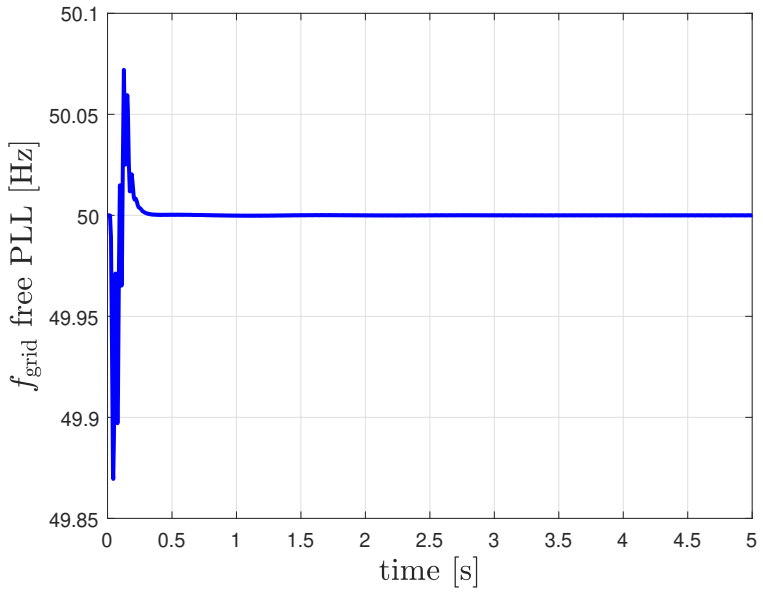

Figure 41: Free PLL Grid frequency

4.4 Conclusion

After studying the grid following and two grid forming strategies, we need to conclude by comparing these different strategies under normal operating conditions.
The first parameter to compare is the response time:

- Grid following: 10 seconds for active power and 3 seconds for reactive power.
- Grid forming VSM: 1 second for both active and reactive power.
- Grid forming Free PLL: 1.5 seconds for both active and reactive power.

The second parameter to observe is the final power values. All three strategies correctly tend towards 2 MW for active power.
For reactive power, the three strategies give different results. As the grid following strategy is controlled using an LQR controller, the reactive power is zero. However, for the grid forming strategies, reactive power is not directly controlled. This leads to good compensation with the VSM strategy, resulting in 0.2 MVAR, while the Free PLL strategy results in 0.4 MVAR. It is important to note that this variation comes from the currents, as the d-axis component of the voltages is correctly maintained at zero.

5 Effects of faults on 380MW network

In this section, I will analyze the impact of various electrical faults, such as subharmonics, reverse voltage injection, and short circuits, on power systems. The objective is to test these faults under different control strategies grid-forming and grid-following and compare their responses. This comparison will help to evaluate the strengths and weaknesses of each control approach in maintaining system stability and performance during fault conditions.

5.1 List of faults

Three phases circuit

A short circuit in a power system occurs when an unintended low-resistance path is created, allowing excessive current to flow. This can happen due to equipment failures, insulation breakdown, or external factors like fallen power lines. The high current can cause significant damage to equipment, trigger protective devices, and lead to power outages. Short circuits are dangerous and can result in voltage dips, fires, or explosions, making it crucial to quickly detect and isolate the fault to protect the network and ensure safety.

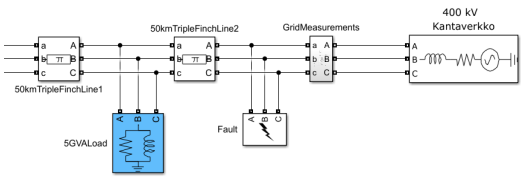

Figure 42: Implementation of Three phases fault

Injection of inverse voltage

Reverse voltage injection occurs when voltage flows in the opposite direction in a power system, typically due to inverter malfunctions, electrical faults, incorrect switching, or transformer backfeeding.

This can lead to equipment damage, interference with protection systems, and power quality issues. It is usually avoided through careful design and operational controls.

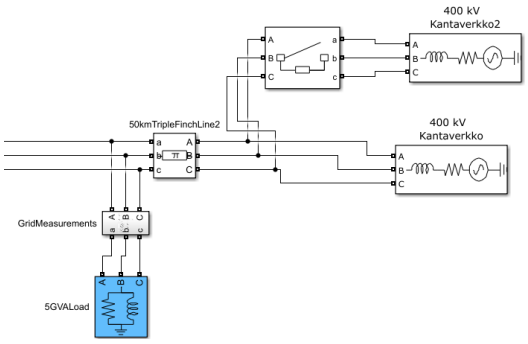

Figure 43: Implementation of injection of inverse voltage

5.2 Comparison of grid control strategy

5.2.1 Three phases short circuit

At 5.02 seconds, the transmission line experiences a three-phase short circuit for 150 ms. Figure 44 one can observe the different frequency responses at the point of common coupling with the short circuit. We can directly see that the frequency variation is smaller in grid forming, with a variation of around 1 Hz compared to 2 Hz for grid following. However, it should be noted that these are still relatively small variations. It should also be noted that the return to normal is slightly faster in grid following and Free PLL compared to VSM.

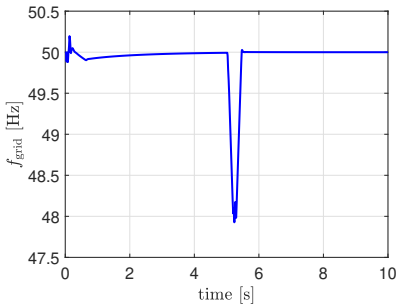

(a) Frequency grid following

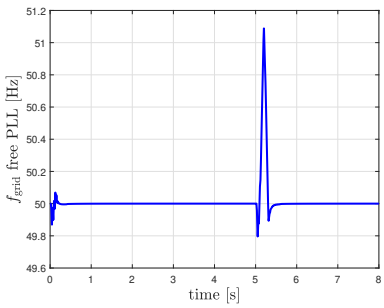

(b) Frequency grid free pll

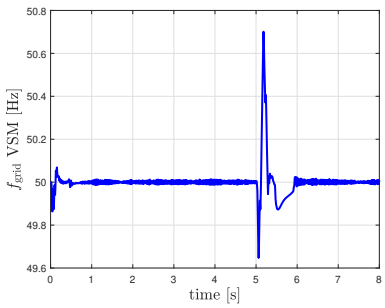

(c) Frequency grid VSM

Figure 44: Frenquency of different control strategy during short circuit

Let us now examine the active and reactive power responses during the short circuit. Figure 45 shows that the active power drops to zero and is compensated by an injection of approximately 0.7 MVAR of reactive power thanks to the LQR corrector. The return to normal is very rapid after the short circuit.

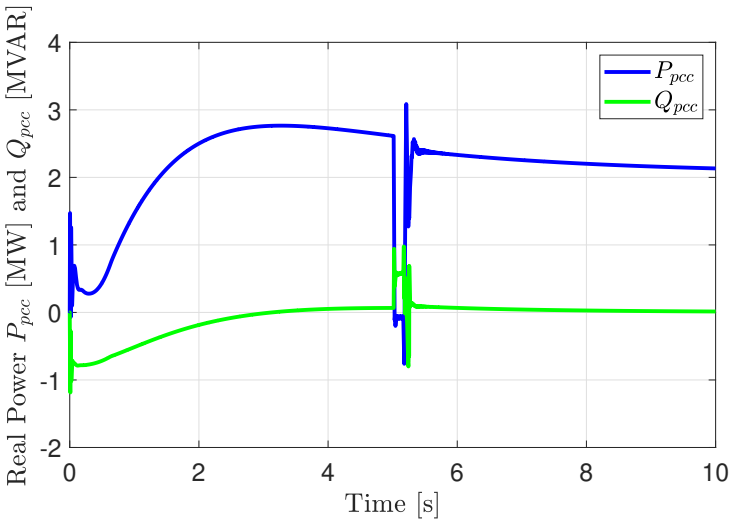

Figure 45: Grid following active and reactive power during short circuit

Figure 46 shows the response of Free PLL, which includes significant power spikes at time $t = 0$ during the short circuit. However, these spikes do not appear in the frequency response. We could implement a power saturation mechanism to minimize these spikes during the short circuit. There is no disturbance rejection since there is no compensating controller, and finally, the return to normal takes approximately 0.5 seconds.

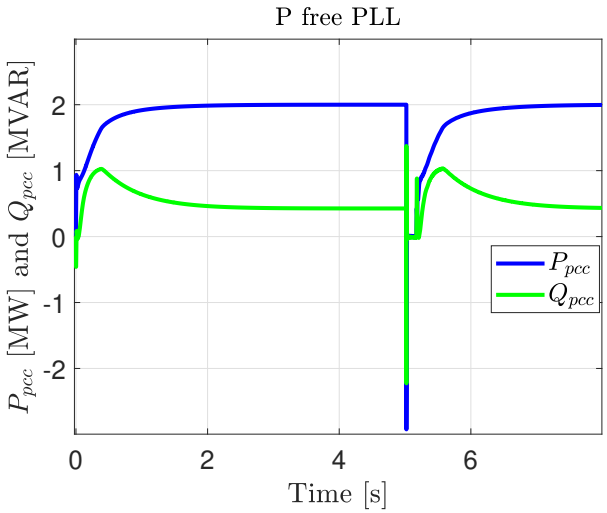

Figure 46: free PLL active and reactive power during short circuit

Figure 47 shows that there are also power spikes, although they are less significant than those observed with Free PLL. There is no disturbance rejection, and the return to normal is somewhat faster than with Free PLL.

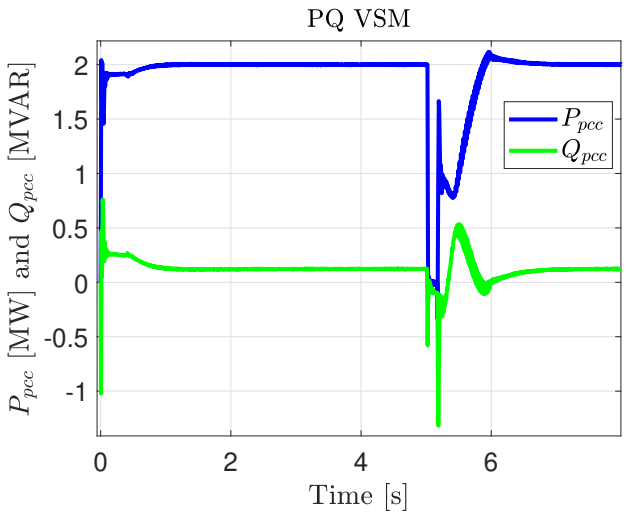

Figure 47: VSM active and reactive power during short circuit

So, even though the Grid Following takes longer to stabilize in steady-state compared to the Grid Forming, its LQR controller allows it to perform better during short circuits.

Let us now consider what happens on the grid side. Figure 48 shows that, at first glance, the responses of the different strategies at the load terminals placed on the grid between the wind park and other energy sources are similar,all sizes set to zero on short circuit. However, when zooming in on the voltage response, the results are notably different.

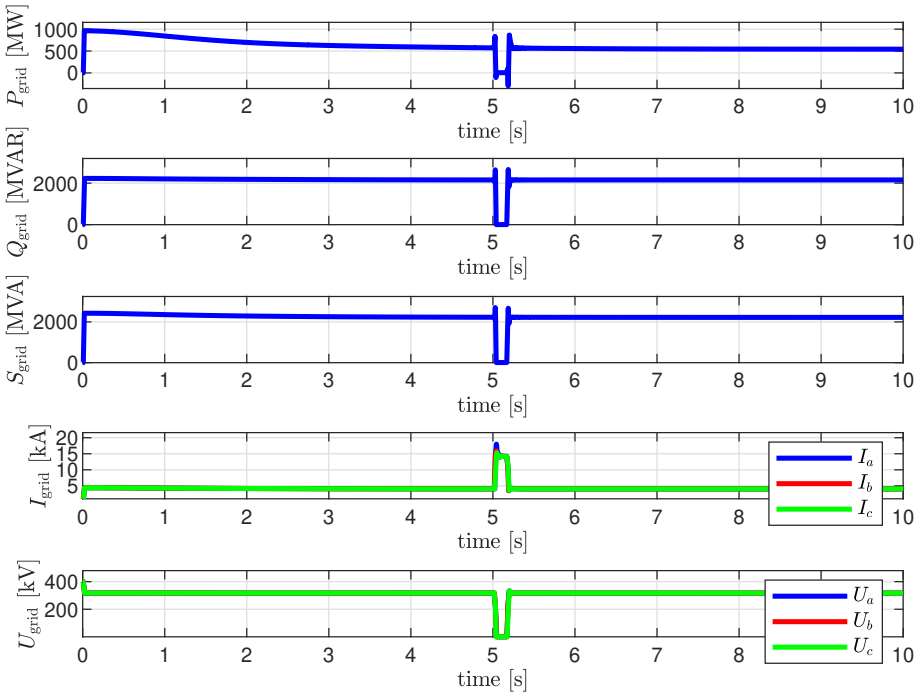

Figure 48: Complete system real with disturbance At 5.02 second. Transmission line powers,voltage and currents in case the wind

The maintenance of the electrical grid is subject to certain rules [17]. To stay connected and operate within the specified voltages and time periods, one must refer to the grid code, shown in Figure 49 (a).
During the short circuit, the voltages of the different strategies are represented with respect to U/U_n, where the nominal voltage is 0.25 MV:

- Grid Following: [5700 V; 8320 V] $\rightarrow$ [2.3%; 3.4%].
- VSM: [1200 V; 3000 V] $\rightarrow$ [0.46%; 1.2%].
- Free PLL: [700 V; 2500 V] $\rightarrow$ [0.02%; 1%].

The time t_1 represented in the grid code is defined based on the network's power. In Finland, this time t_1 does not exceed 200 ms. Therefore, based on the values obtained after this time t_1, the electrical grid would need to be disconnected.

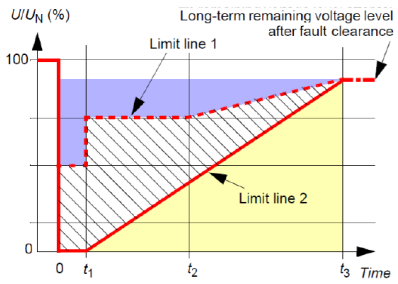

(a) Grid codes may require from production unit

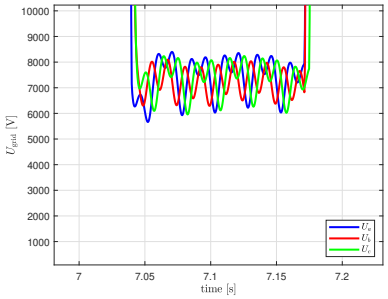

(b) Grid Voltage response of Grid following

Figure 49: Grid code and voltage grid measurements

5.2.2 Injection Inverse Voltage

For this fault, a reverse voltage of -10^5 V will be injected into the network, over a period of 0.5sec. As with the short circuit simulation, we can see from the frequency response Figure 50 that the grid following is much more sensitive to disturbance from the grid, with almost 4Hz of variation compared with 1Hz for the VSM and only 0.2Hz for the free PLL.

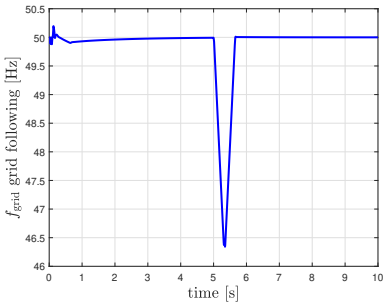

(a) Frequency grid following

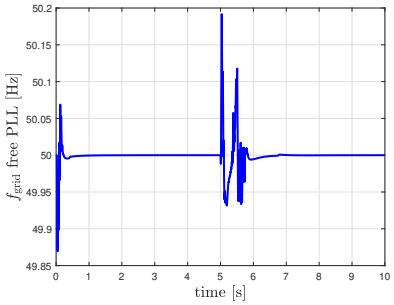

(b) Frequency free-PLL

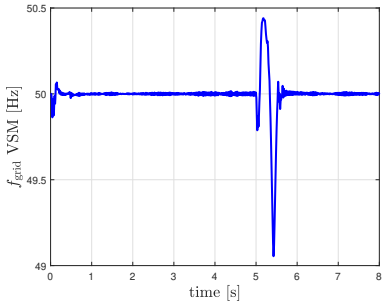

(c) Frequency VSM

Figure 50: Frenquency of different control strategy during injection of inverse voltage

During the power analysis, we observe that active and reactive power do not react the same way when reverse voltage is injected. The difference in their reactions arises from the fact that active power is related to the real energy flow between the generator and the load, while reactive power is associated with the energy stored and exchanged between the system's inductive and capacitive elements. When reverse voltage is injected, it primarily affects the reactive components, altering the amount of stored and exchanged energy, while active power is less influenced by transient variations and remains more stable.

Figure 51 We can see that the active power reacts much more than the reactive power and both are subject to sub harmonic during the fault. And quickly returns to normal after the fault

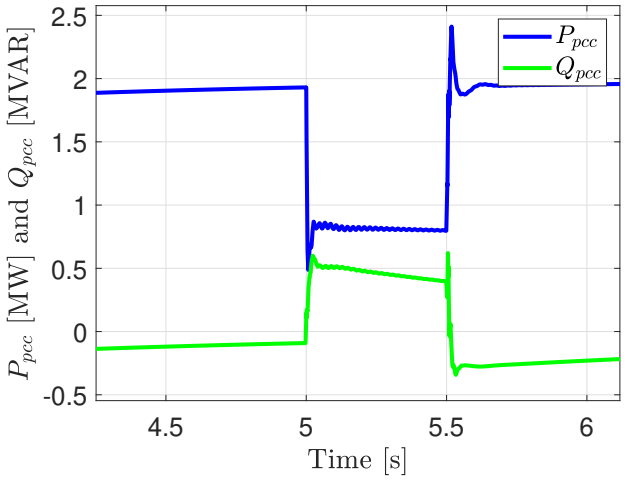

Figure 51: Grid following active and reactive power during injection of $-1 \cdot 10^5$

Figure 52 We observe that the same power spikes as during the short circuit Figure 46, during the fault we observe that the power is also subject to sub harmonics and noise, and the return to normal takes even longer than during the short circuit.

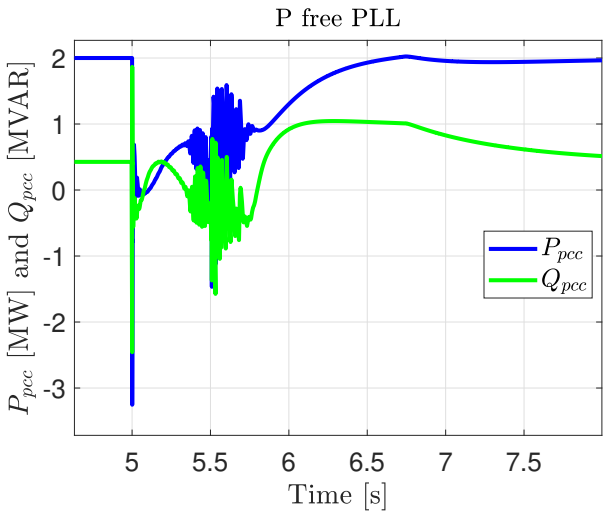

Figure 52: Free PLL active and reactive power during injection of $-1 \cdot 10^5$

Figure 53 We observe that the VSM strategy is also subject to sub-harmonics but quickly returns to normal after the fault.

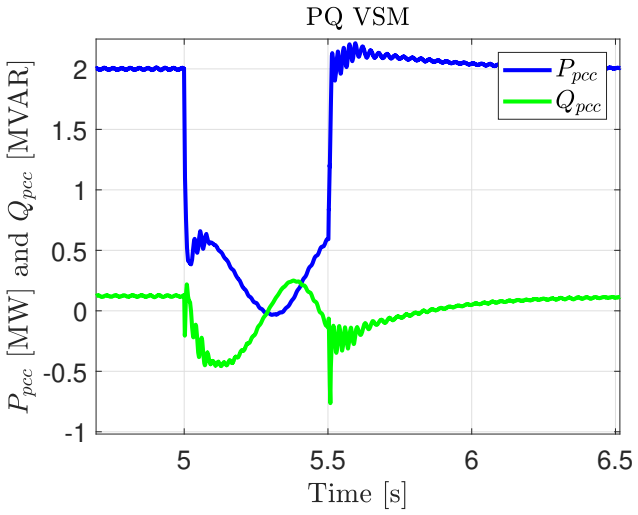

Figure 53: VSM active and reactive power during injection of $-1 \cdot 10^5$

To conclude on the robustness of the systems during reverse voltage injection, let us observe Figure 54, which shows the grid active power for the different strategies. We observe that the Free PLL response is the best, with small oscillations and the highest power maintained. VSM is subjected to a significant sub-harmonic, making its response unsatisfactory. Finally, the Grid Following strategy has the lowest power but with small oscillations.

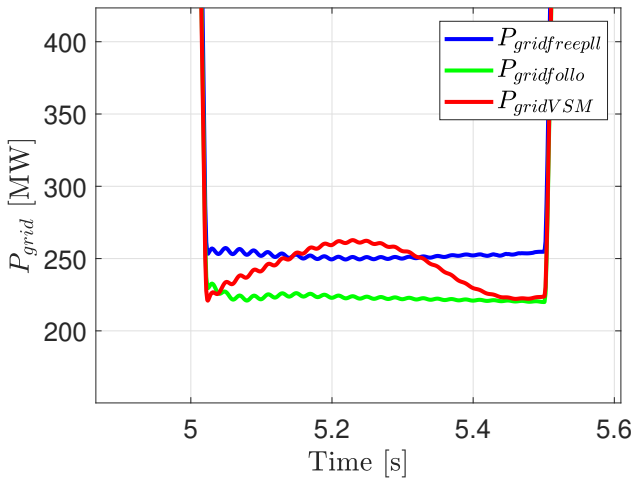

Figure 54: Grid Power during faults

5.2.3 Conclusion

To conclude on grid faults, we can note that each strategy has its strengths and weaknesses. For instance, the Grid Following strategy has the particular advantage of injecting active power to reject various faults, and its LQR controller with state feedback allows the system to return to normal more quickly. However, the frequency variations are higher compared to Grid Forming, which is significant since maintaining grid frequency is crucial for the proper operation of the electrical network. As mentioned in the introduction, both strategies should be combined to form the optimal control system. For example, a wind farm could consist of 40% Grid Following and 60% Grid Forming to achieve the best performance.

6 Digital twin of the wind power conversion

The digital twin of the wind farm aims to evaluate the operating point of the energy conversion chain up to the common coupling point. This assessment must take into account the fluctuation of wind speed and the network monitoring strategy. Since the digital twin is connected to an entire power grid, it must be computationally lightweight while still providing high accuracy. After identifying the two transfer functions (active and reactive power) for each control strategy (grid-following, grid-forming with Free-PLL, and VSM), their transient and short-circuit responses will be presented and compared to the real system.

6.1 Development of the digital twin

In order to reproduce accurately the transient during either the intermittent wind energy or the grid faults, the digital twin can be constructed from the active and reactive power control reference. The full system enables to derive equivalent dynamic model of power at the point of common coupling. The synoptic in Figure 55 presents the concept of the digital twin.

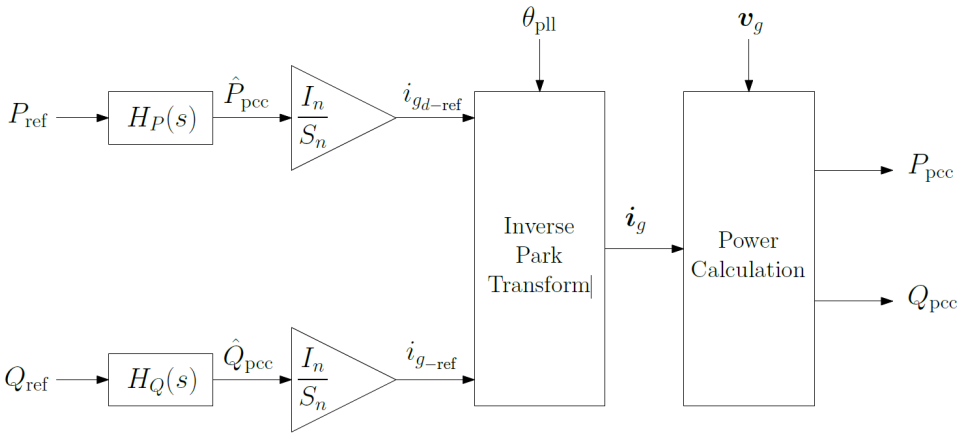

Figure 55: Representation of the digital twin for modeling the wind farm from the turbine to the point of common coupling.

This model requires the derivation of the transfer function $H_P(s)$ and $H_Q(s)$ which represents the dynamics of active and reactive power control. In the complete system, active power is controlled by the pitch angle and d-axis current of the generator, while reactive control is regulated by the q-axis voltage of the inverter. In order to perform the transformation to the three physical phases, the inverse Park transform can be used with phase loop locking for grid-following or with active power control for grid-forming.
The choices I made to create these simplified models are based on second-order transfer functions, identified using the ident function in MATLAB, and then implemented in Simulink. These transfer functions are represented by the Laplace variable s.

6.2 Grid-following Digital Twin

The grid-following controller regulates the reactive power at the point of common coupling (PCC) and the DC bus voltage. In this simplified model, the DC bus voltage regulation is replaced by active power regulation. The active power at the PCC is controlled by the turbine pitch angle and the generator's d-axis current. To simplify the energy conversion chain, we replicate the active power dynamics using the control of the d-axis current in the digital twin.
Both the active and reactive power regulation are modeled by second-order systems with unit gain. The transfer functions are given by:
Active Power Transfer Function:

$$H_{Pfollowing}(s) = \frac{P_{pcc}}{P_{ref}} = \frac{\alpha_1 \alpha_2}{(s+\alpha_1)(s+\alpha_2)} \tag{31}$$

where the real poles are $-\alpha_1 = -\alpha_2 = -0.8677$ rad/s identified from the active power response of the full system.
Reactive Power Transfer Function:

$$H_{Qfollowing}(s) = \frac{Q_{pcc}}{Q_{ref}} = \frac{\alpha^2 + \omega_d^2}{(s+\alpha)^2 + \omega_d^2} \tag{32}$$

where $\alpha = 0.818$ rad/s and $\omega_d = 1.214$ rad/s.

You can observe Figure 56 the frequency is stable at 50 Hz in steady state.

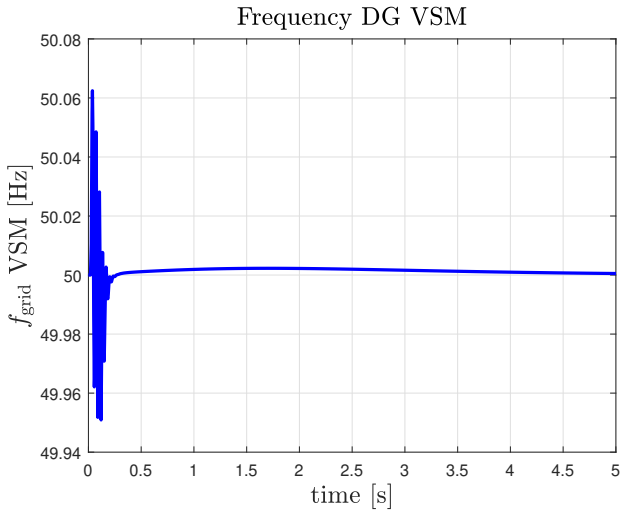

Figure 56: Frequency response for grid-following digital twin

Let's now compare the power response from Figure 28 with the real system in Figure 28. The response time and final value are accurate but there is no overshoot in reactive power, unlike what is observed in the real system.. We do not observe any variation in reactive power because the initialization of the DC bus does not follow the reference; it directly concerns reactive power rather than the DC bus voltage.

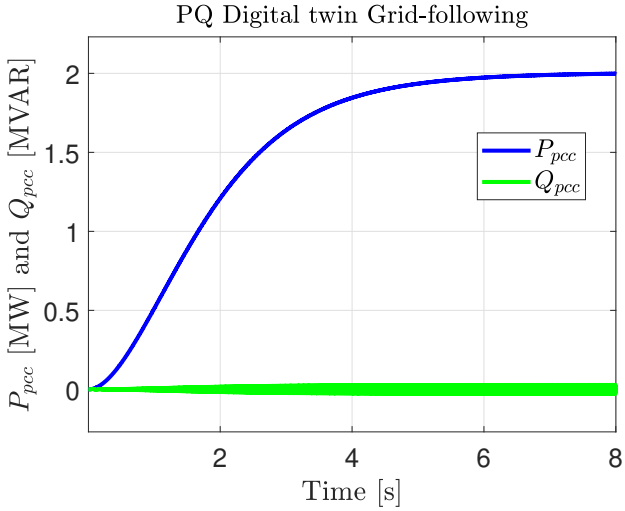

Figure 57: Step response grid-following digital twin (Active and Reactive power)

6.3 Grid-forming Digital Twin

6.3.1 Virtual Synchronous Machine Digital Twin

In the Virtual Synchronous Machine (VSM) strategy, both the active and reactive power regulation are modeled by second-order systems. The active power is controlled by the generator's d-axis current to mimic the dynamics of a synchronous machine.

Active Power Transfer Function:

$$H_{PVSM}(s) = \frac{P_{pcc}}{P_{ref}} = \frac{\frac{K}{\omega_n^2}}{s^2 + 2\xi\omega_n s + \omega_n^2} \tag{33}$$

with $K = 285; \omega_n = 17.12\text{rad/s}; \xi = 3.48;$

Reactive Power Transfer Function:

$$H_{QVSM}(s) = \frac{Q_{pcc}}{P_{ref}} = \frac{\frac{(s-\alpha_3)(s-\alpha_4)}{\omega_n^2}}{s^2 + 2\xi\omega_n s + \omega_n^2} \tag{34}$$

with $\alpha_3 = 148.5\text{rad/s}; \alpha_4 = 16.5\text{rad/s}; \omega_n = 41.11\text{rad/s}; \xi = 4.95;$

We can observe Figure 58 that the frequency response is not exactly the same as that shown in the figure Figure 36; the frequency peak is higher with the digital twin, but the response appears less noisy.

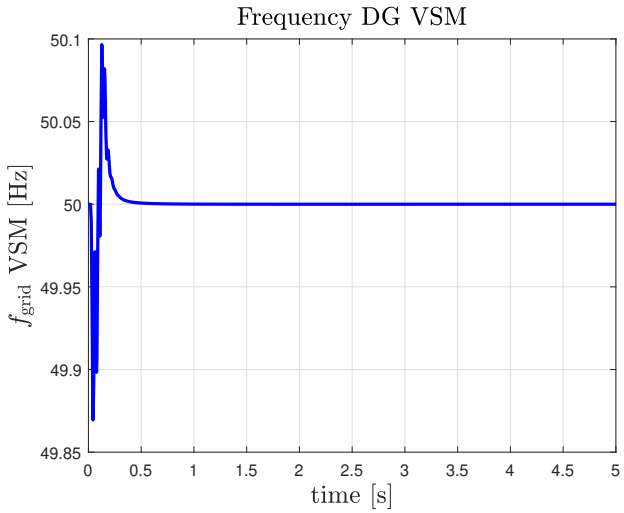

Figure 58: Frequency response for VSM digital twin

Let's focus on the power response of the VSM digital twin Figure 59. Both power values match the final value shown in Figure 36. The transient behavior of the powers is slightly different from that of the real system, with, for example, a higher reactive power peak. However, since the system stabilizes very quickly, these transient behaviors will not be visible on the grid.

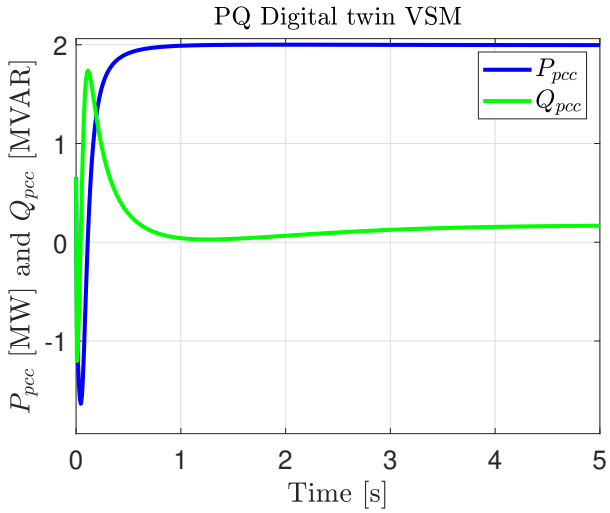

Figure 59: Step response VSM digital twin (Active and Reactive power)

6.3.2 Free-PLL Digital Twin

In the grid-forming (Free-PLL) strategy, the active and reactive power regulation follows a second-order system dynamic. The active power control is directly managed by the generator's d-axis current, while the reactive power response is characterized by underdamped behavior.

Active Power Transfer Function:

$$H_{Pfreepll}(s) = \frac{P_{pcc}}{P_{ref}} = \frac{\frac{\alpha_5 s + \alpha_6}{\omega_n^2}}{s^2 + 2\xi\omega_n s + \omega_n^2} \tag{35}$$

with $\alpha_5 = 233.5\text{rad/s}; \alpha_6 = 3.4 \cdot 10^3\text{rad/s}; \omega_n = 58.65\text{rad/s}; \xi = 9.38;$

Reactive Power Transfer Function:

$$H_{Qfreepll}(s) = \frac{Q_{pcc}}{P_{ref}} = \frac{\frac{(\alpha_7 s + \alpha_8)}{\omega_n^2}}{s^2 + 2\xi\omega_n s + \omega_n^2} \tag{36}$$

with $\alpha_7 = 19.0\text{rad/s}; \alpha_4 = 12.9\text{rad/s}; \omega_n = 3.56\text{rad/s}; \xi = 1.07;$

We can observe Figure 60 that the frequency response is exactly the same as that shown in the figure Figure 41.

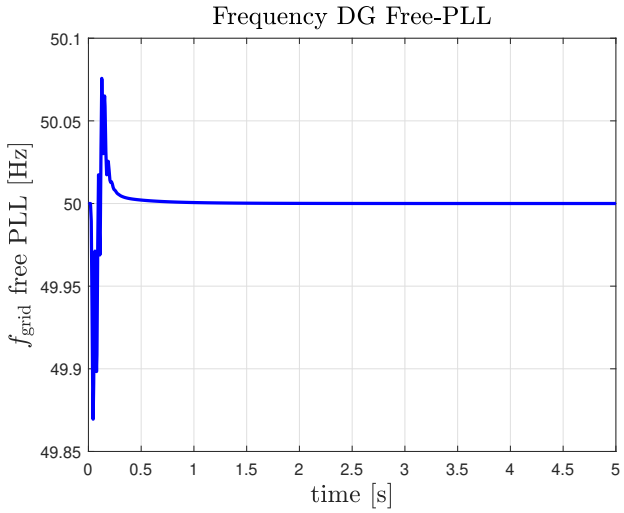

Figure 60: Frequency response for Free-PLL digital twin

The power responses Figure 61 closely match those of the real system Figure 40, with the same response time and final value for active power. The only issue is that the peak and final value of reactive power are higher than normal, which could potentially cause problems when the plant supplies apparent power exceeding the required amount. This is a recurring issue in grid-forming strategies, as reactive power is not controlled and thus not zero.

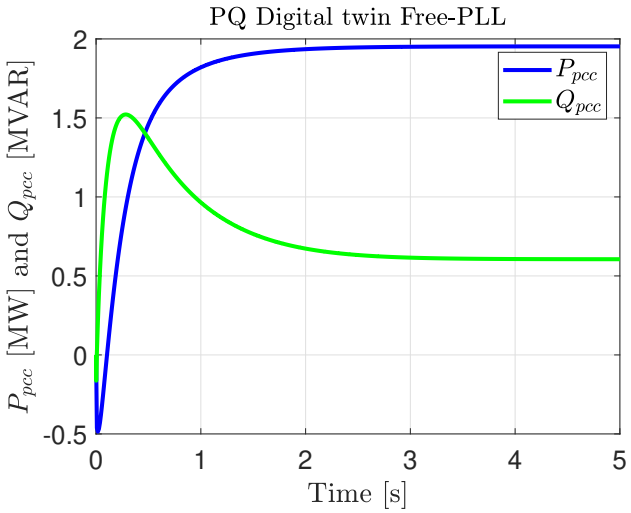

Figure 61: Step response Free-PLL digital twin Active and Reactive power

6.4 Comparison between the real system and the digital twin during a short circuit.

Let's now examine the frequency response of the digital twins Figure 62 compared to the grid frequency of the real systems Figure 44. We observe that the responses have a similar shape but with a higher fault amplitude for the digital twin. This is not very concerning because if the digital twin accepts the fault during several tests, the real system will also accept it, as the amplitude of the frequency of the same fault will be less significant in the real system.

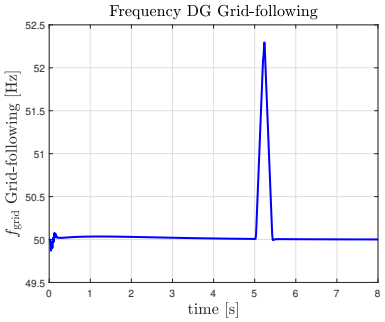

(a) Frequency grid following

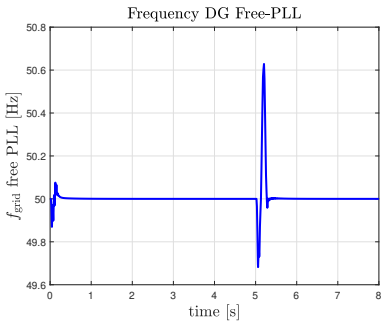

(b) Frequency grid following

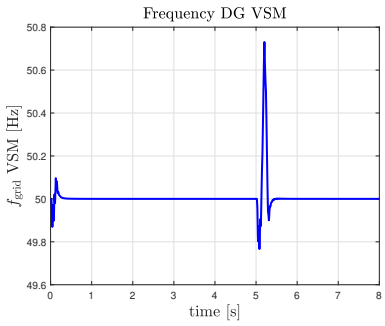

(c) Frequency VSM

Figure 62: Frenquency of different digital-twin during short-circuit

The power response of the digital twin Figure 63 injects more reactive power than the real system

Figure 45. Additionally, we can observe that the peaks of this reactive power are much higher compared to the real system.

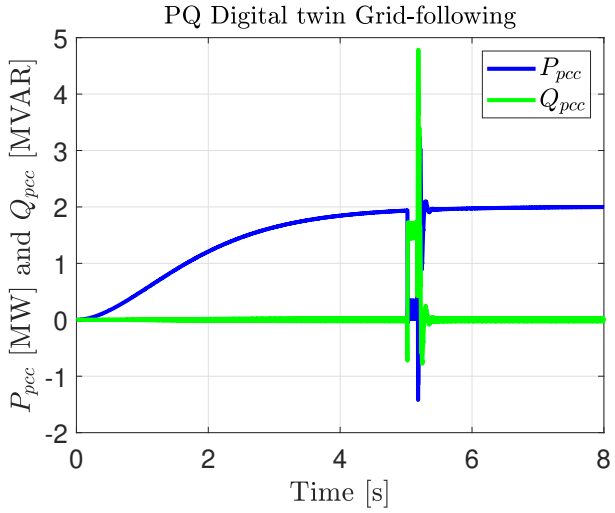

Figure 63: Grid following active and reactive power during short circuit

For the response during the short circuit of the Free PLL strategy Figure 64, it is similar to the real system Figure 46 in terms of response time. Differences are observed with lower peaks compared to the real system during fault activation, but with peaks during the return to normal that are not present in the real system. Overall, the Free PLL digital twin is functional and accurate during faults.

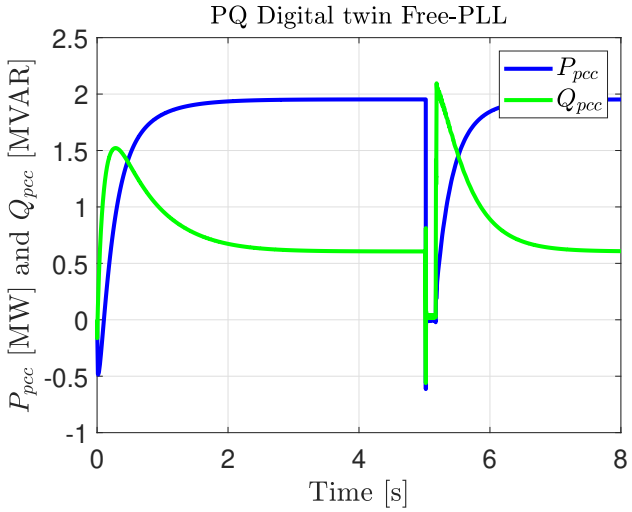

Figure 64: free PLL active and reactive power during short circuit

For the comparison between the digital twin Figure 65 and the real system Figure 47 of the VSM strategy, the comments are the same as for the Free PLL strategy: similar response times, lower fault activation peaks, and higher peaks during the return to normal. In my opinion, the VSM digital twin is the one that best reflects the real system.

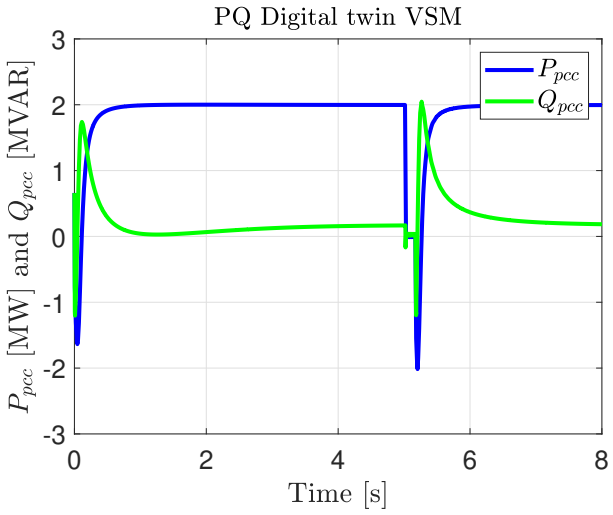

Figure 65: VSM active and reactive power during short circuit

Part IV
Conclusion

This report covers the entire duration of my 20-week internship, which is why it is longer than requested. The objective of this report was to model the control strategies for Finnish wind farms and to test fault scenarios to assess the robustness of the different control strategies. We observed that the various grid-forming strategies are robust and similar with and without PLL, while the grid-following strategy is also robust due to its LQR controller, which allows for reactive power injection during grid faults. In practice, these two strategies (grid-following and grid-forming) work together to achieve the best performance and efficiency possible.

The main issue with these simulations is their duration, with each simulation taking between 20 and 40 minutes, which is impractical for someone wishing to simulate the entire Finnish electrical grid (all possible sources). Therefore, the end of my internship was devoted to developing an equivalent model for each strategy using MATLAB's identification function and finding a second-order transfer function model. After this implementation, I can conclude that the simplified models behave similarly to the full models, with the same response times, final values, and accurate representation of grid fault responses. The advantage is that simulation time is reduced to 1 or 2 minutes, allowing my colleagues in the electrical grid sector to simulate the two smart grid strategies reliably and efficiently.

Part V
Appendix

A Virtual impedance code

```
function [deltaegd, deltaegq] = virtualimpedance(Isd, Isq, In, kpRVI,
    oXR)
    % This function calculates the modified AC voltage references egdstar and
    egqstar
    % Inputs:
    %   Isd  - d-axis component of the converter current
    %   Isq  - q-axis component of the converter current
    %   In   - Nominal current value
    %   kpRVI - Virtual impedance proportional gain
    %   oXR - Virtual impedance ratio
    %   egd  - Original d-axis component of the AC voltage reference
    %   egq  - Original q-axis component of the AC voltage reference
    % Outputs:
    %   egdstar - Modified d-axis component of the AC voltage reference
    %   egqstar - Modified q-axis component of the AC voltage reference

    % Calculate delta I
    deltaI = sqrt(Isd 2 + Isq 2) - In;

    % Calculate virtual impedance values
    if deltaI ¿ 0
        XVI = kpRVI * oXR * deltaI;
        RVI = XVI / oXR;
    else
        XVI = 0;
        RVI = 0;
    end

    % Calculate voltage drops due to virtual impedance
    deltaegd = RVI * Isd - XVI * Isq;
    deltaegq = RVI * Isq + XVI * Isd;


end
```

Listing 1: Virtual impedance

B Current saturation

```
function [isdqsd, isdqsq] = CSA(isdstar, isqstar, ImaxSAT)
% Calculate the current vector amplitude
isdqsmag = sqrt(isdstar 2 + isqstar 2);

% Check if the current amplitude is below the saturation limit
if isdqsmag ¡ ImaxSAT
    % No saturation needed
    isdqsd = isdstar;
    isdqsq = isqstar;
```

```
else
   % Saturation needed
    % Calculate the angle
    theta = atan2(isqstar, isdstar);

   % Apply saturation
    isdqsd = ImaxSAT * cos(theta);
    isdqsq = ImaxSAT * sin(theta);
end

return
```

Listing 2: Virtual impedance

References

[1] Floran Martin,Robert John Millar, and Janne Sepännen, *Digital twin of a wind farm equipped with type IV generator and a grid following controller*. SINARP project, 2023.

[2] Fingrid, *Electricity System of Finland*. Fingrid, 2023.

[3] Avazov, A., *AC Connection of Wind Farms to Transmission System: From Grid-Following to Grid-Forming*. Electric Power. Centrale Lille Institut; Katholieke Universiteit te Leuven, Faculteit Geneeskunde, 2022.

[4] National Renewable Energy Laboratory, *Dynamic Models for Wind Turbines and Wind Power Plants*, NREL/SR-5500-52780, 2013.

[5] Enercon Technology, *Website*, 2023.

[6] Heier, S., *Grid Integration of Wind Energy: Onshore and Offshore Conversion Systems*, Wiley, 2014.

[7] Li, F., Zhang, X., Zhu, H., Li, H., and Yu, C., *An LCL-LC Filter for Grid-Connected Converter: Topology, Parameter, and Analysis*, IEEE Transactions on Power Electronics, vol. 30, no. 9, pp. 5067-5077, Sept. 2015.

[8] Zhang, C., Dragicevic, T., Vasquez, J. C., and Guerrero, J. M., *Resonance Damping Techniques for Grid-Connected Voltage Source Converters with LCL Filters — A Review*, ENERGYCON, Croatia, 2014, pp. 169-176.

[9] Wu, W., et al., *A Robust Passive Damping Method for LLCL-Filter-Based Grid-Tied Inverters to Minimize the Effect of Grid Harmonic Voltages*, IEEE Transactions on Power Electronics, vol. 29, no. 7, pp. 3279-3289, July 2014.

[10] Kaura, V., and Blasko, V., *Operation of a Phase Locked Loop System under Distorted Utility Conditions*, IEEE Transactions on Industry Applications, vol. 33, no. 1, Jan.-Feb. 1997.

[11] Franklin, G. F., Powell, J. D., and Emami-Naeini, A., *Feedback Control of Dynamic Systems*, 7th ed., Prentice Hall, 2014.

[12] Hespanha, J. P., *Lecture Notes on LQR/LQG Controller Design*, 2005.

[13] Qoria, T., and Rokrok, E., *A PLL-Free Grid-Forming Control with Decoupled Functionalities for High-Power Transmission System Applications*, 2020.

[14] Machowski, J., Bialek, J. W., and Bumby, J. R., *Power System Dynamics and Stability*, Wiley, Chichester, UK, 1997. (Chapters 2 and 5)

[15] D'Arco, S., Suul, J. A., and Fosso, O. B., *A Virtual Synchronous Machine Implementation for Distributed Control of Power Converters in Smart Grids*, 2015.

[16] Dinesh Pattabiraman* ,R. H. Lasseter, T. M. Jahns., *Comparison of Grid Following and Grid FormingControl for a High Inverter Penetration Power System*, 2018.

[17] Marko Hinkkanen, Mikko Routimo, *AAlto courses Grid Faults and Disturbances ELEC-E8402 Control of Electric Drives and Power Converters*